PART I

MODELING OF THE MICROWORLD

CHAPTER 1

MICROWORLD MODELING IN VACUUM AND GASEOUS ENVIRONMENTS

PIERRE LAMBERT and STÉPHANE RÉGNIER

1.1 INTRODUCTION

1.1.1 Introduction on Microworld Modeling

This first part describes the physical models involved in the description of a micromanipulation task: adhesion, contact mechanics, surface forces, and scaling laws. The impact of surface roughness and liquid is discussed later on in Chapter 2.

The targeted readership of Chapters 1 and 2 is essentially composed of master's degree students and lecturers, Ph.D. students, and researchers to whom this contribution intends:

- To give the theoretical background as far as the physics and scaling laws for micromanipulation are concerned
- To propose design rules for micromanipulation tools and how to estimate the interaction force between a component and the related gripper or between a cantilever tip and a substrate

The goal of developing models may be questioned for many reasons:

- The task is huge and the forces dominating at the micro- and nanoscale can only be modeled very partially: for example, some of them cannot be modeled in a quantitative way (e.g., hydrogen bonds) suitable for robotics

Robotic Microassembly, edited by Michaël Gauthier and Stéphane Régnier

purposes, most of the proposed models are only valid at equilibrium (at least all the models based on the derivation of surface or potential energies).

- The parameters involved in the existing models are sometimes impossible to know, such as, for example, the electrical charge distribution on a dielectric oxide layer.
- Maybe as a consequence of the previous reason—that is, a full characterization is impossible—the micro- and nanoscale specifically suffer from a very large experimental dispersion, which makes the model refinements questionable. According to own experience, experimental results are difficult to keep within a few tens of a percent error interval. Yang and Lin [93] recently write that *the measurements usually show poor reproducibility*, suggesting that *the major causes of irreproducibility can be roughness and heterogeneity of the probe surface and sample*.

Nevertheless the use of—even basic—models helps the microrobotician to get into the nonintuitive physics dominating the microworld—mainly adhesion-related instabilities such as pull-in and pull-out—to give an explicating scheme of the experiments—what is the role of humidity? what is the influence of the coatings—to design at best grippers and tools on a comparative way—no matter the exact value of the force; but a geometries comparison leads to the best design. These advantages will be detailed later on.

Classical adhesion models [20, 41, 67] usually proposed to study adhesion in micromanipulation or atomic force microscopy (AFM) are based on the elastic deformation of two antagonist solids (microcomponent/gripper in micromanipulation, cantilever tip/substrate in AFM). This part will introduce models that are now well known, but they will be introduced in the framework of microassembly. Modern models will refer to recent developments and/or recent papers. The theoretical background proposed in this part aims at detailing:

1. Every phenomenon leading to a force interaction: capillary forces, electrostatic forces (in both liquid and air environment, but restricted to conductive materials), van der Waals forces, and contact forces
2. The influence of surface science concepts such as topography, deformation, and wettability

These elements constitute a basis on which to model adhesion without using empirical global energy parameters such as surface energies.

When dealing with stiction and adhesion problems in micromanipulation, one is often referred to a list of many concepts (van der Waals interaction, capillary force, adhesion, pull-off), which sometimes can recover one another. Lambert and Régnier [53] have proposed to sort out these forces by making the distinction whether there is contact or not. When there is no physical contact between two solids, the forces in action are called distance or surface forces (according to the scientific literature in this domain [12, 22, 76], these latter are electrostatic, van der Waals, and capillary forces). When both solids contact one another, there is

TABLE 1.1. Forces Summary and Their Interaction Distances

Interaction Distance	Predominant Force
Up to infinite range	Gravity
>From a few nm up to 1 mm	Capillary forces
>0.3 nm	Coulomb (electrostatic) forces
0.3 nm < separation distance < 100 nm	Lifshitz–van der Waals
< 0.3 nm	Molecular interactions
0.1–0.2 nm	Chemical interactions

deformation and adhesion forces through the surfaces in contact. In this case, the authors considered contact forces and adhesion or pull-off forces. Electrostatic or capillary effects can be added, but van der Waals forces are not considered anymore because they are thought already involved in the pull-off term. The new idea conveyed in this part is to consider van der Waals, capillary,[1] and electrostatic forces as parts into which the global pull-off force can be split.

Beside these contact or close to contact forces, it is also important to focus on other forces that affect the dynamics of small components. This description can only be done by considering the specificities of the working environment. In liquid environments, for example, we will consider viscous drag (Lenders et al. [58] have recently presented a design of microfeeder using these forces), electrostatic double-layer effects, and (di)electrophoresis. Very recently, a new focus has been found on the effect of gas bubbles in liquid media.

Additionally, we will try to address the question of mechanical contact from two points of view: what are the limits of the Hertz-based models [20, 41, 67] and what is the influence of a liquid environment on this contact?

1.1.2 Microworld Modeling for Van der Waals Forces and Contact Mechanics

The first chapter concerns vacuum or gaseous environments. First in Section 1.2 some well-accepted models are recalled, concerning van der Waals forces, elastic contact mechanics and the related adhesion models, and capillary force models at the submillimetric scale. Second, in Section 1.3 very recent published results are presented together with our own perspective: capillary condensation effects, the influence of surface roughness, and mechanical deformation on electrostatic forces.

Before going through these models, let us mention that many (attractive) effects contribute to adhesion. Based on Lee [57], we propose the schematic forces summary presented in Table 1.1.

Additional effects turn out to be also of importance: Let us cite the Casimir effect, which will not be detailed in this contribution. We refer to Klimchitskaya and Hostepanenko [45].

[1]Capillary forces will be considered at the submillimetric scale [50] and at the nanometric scale [16].

It seems, however, that capillary effect dominates all the microworld from a few nanometers up to tenths of millimeters van der Waals effects turn out to compete with capillary effect but only within the nano range up to a few tens of nanometers (we can consider the limit of the retardation effect as the limit, see later on). We therefore mainly focus on both effects together with the electrostatic adhesion, which comes from either the intense electrostatic fields coming from microrobotic actuation—they can be avoided using thermal actuation—or from the moderate effect of contact potentials.

1.2 CLASSICAL MODELS

1.2.1 Van der Waals Forces

The so-called van der Waals forces are often cited in papers dealing with micromanipulation and microassembly, probably because the founding papers of these bibliography reviews [12, 22] present these forces next to the capillary and the electrostatic forces as being of the utmost importance in the sticking of microparts. Other authors [7] prefer to neglect these forces because they are of a smaller order. The reasons for this opposition do not seem to be clear, all the more so since some authors propose to use it as a suitable gripping principle [3, 23]. The will to clarify this situation is a first reason to study van der Waals forces. A second reason lies in the fact that most force expressions used in the literature on microassembly are only approximations of simplified geometries (spheres and planes). If these approximations are sufficient for experimental case studies, the influence of more complex geometries (nonsymmetrical geometries) including roughness profiles should be studied for many applications. We propose to briefly present the physical underlying phenomena that explain these forces and to explain the way(s) they can be calculated. An overview of the approximations from the literature is proposed in the conclusion of this section.

A good and very didactic introduction to the subject can be found in Israelachvili [38], while a more exhaustive description of the van der Waals (VDW) forces has also been proposed [1, 26, 39]. In order to explain, at least from a qualitative point of view, the power law describing the van der Waals interaction energy, let us start from the potential energy of an electric charge q (Eq. 1.1) and that of a permanent dipole p made of two charges q and $-q$ separated by a distance l (Eq. 1.2 states if $l << r$), in both cases in a point P at a separation distance r and in vacuum (see Fig. 1.1):

$$U(P) = \frac{1}{4\pi\epsilon_0}\frac{q}{r} \tag{1.1}$$

$$U(P) = \frac{1}{4\pi\epsilon_0}\frac{p\cos\theta}{r^2} \tag{1.2}$$

We see that the potential depends on the inverse of the first power of the separation distance in the case of a charge and on the inverse of the second

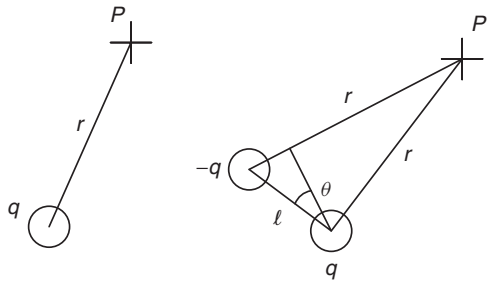

Figure 1.1. Illustration of potentials of a charge and of a permanent dipole.

power in that of a permanent dipole. If we now consider the interaction potential $w(r)$ of two permanent dipoles p_1 and p_2 separated by a distance r, it can be shown [89] that $w(r)$ also depends on the inverse of the third power of the separation distance:

$$w(r) \approx \frac{1}{4\pi\epsilon_0}\frac{p_1 p_2}{r^3} \tag{1.3}$$

We can now introduce the underlying idea to explain the van der Waals forces. Let us consider two molecules, separated by a distance r. If these two molecules are polar (which means that there is a permanent electric dipole inside the molecule due to the fact that the gravity center of the positive charges does not fit with that of the negative forces), their interaction energy can be described by Eq. 1.3. Actually, the van der Waals forces also act between totally neutral atoms and molecules such as helium, methane, and carbon dioxide. This is due to the fact that even in a nonpolar atom, the gravity center of the positive and negative charges are not instantaneously superposed, leading to an instantaneous dipole p_1, with a characteristic charge in the order of the electronic charge e and a separation distance of about one atom radius a_0 (note that this explanation was first applied by D. Tabor to the interaction between two Bohr atoms, a_0 known as the first Bohr radius):

$$p_1 \approx a_0 e \tag{1.4}$$

If the considered molecules are polarizable, this instantaneous dipole will polarize the neighboring atom, and consequently produce a dipole p_2 given by

$$p_2 \approx \alpha\frac{1}{4\pi\epsilon_0 r^3}a_0 e \tag{1.5}$$

where α is the polarizability of the second atom, defined by

$$\alpha \approx 4\pi\epsilon_0 a_0^3 \tag{1.6}$$

The two instantaneous dipoles p_1 and p_2 given by Eqs. 1.5 and 1.6 lead to an interaction potential described by Eq. 1.3:

$$w(r) \approx \frac{1}{4\pi\epsilon_0}\frac{p_1 p_2}{r^3} \approx \frac{\alpha a_0^2 e^2}{(4\pi\epsilon_0)^2}\frac{1}{r^6} \div \frac{1}{r^6} \tag{1.7}$$

This power law holds as far as the orientation (Keesom), the induction (Debye) and the dispersion (London) terms are concerned. Moreover, by assuming these interactions to be additive (= by assuming they do not depend on the surrounding molecules), these three terms can be regrouped:

$$w(r) = \left(-\frac{K_K}{r^6}\right) + \left(-\frac{K_D}{r^6}\right) + \left(-\frac{K_L}{r^6}\right) = -\frac{K}{r^6} \tag{1.8}$$

The so-called retardation effect occurs when the separation distance between the instantaneous dipole and the induced dipole increases over a cut-off length of the order of 5–10 nm: In this case, the traveling time of the electromagnetic wave from the instantaneous dipole and the induced dipole become bigger and, consequently, both dipoles lose their coherence, leading to an energy reduction. The decrease with the separation distance occurs faster and it is assumed that it can be described according to

$$w(r) = -\frac{K_R}{r^7} \tag{1.9}$$

The fast decrease of the van der Waals forces explains that they seem to be limited to the atomic domain. Nevertheless, this decrease occurs more slowly when we consider the interaction between two macroscopic bodies (i.e., a body with a very large number of molecules, including bodies that have a size in the order of a few micrometers and that are consequently considered microcomponents when dealing with microassembly terminology). Therefore, it is not so obvious to choose whether these forces have to be dealt with or not.

Let us now have a look on the ways to compute the van der Waals interaction between two macroscopic bodies: The first one is known as the microscopic or Hamaker approach, and the second one is called the macroscopic or Lifshitz approach. From a strictly theoretical point of view, the van der Waals forces are nonadditive, nonisotropic, and retarded. However, London [60] proposed a straight and powerful way to establish the potential interaction by assuming a pairwise additivity of the interactions. Moreover, this approach does not consider the retardation effect. The results are therefore limited to separation distances between an upper limit of about 5–10 nm (because we neglect the retardation effect) and a lower limit of about one intermolecular distance [because Eq. 1.2 that $l << r$. This lower boundary is reinforced by the value of the equilibrium distance (about 0.1–0.2 nm) arising from the Lennard-Jones potential: for separation distances smaller than 0.1–0.2 nm, very strong repulsive forces occur that can no longer be neglected]. This lower limit is sometimes called the van der

Waals radius [38]. We should keep in mind that even with these restrictions, the results are not exactly correct for the interaction of solids and liquids because of the pairwise summation assumption. However, Israelachvili [39] and Russel et al. [78] consider that these approximations are useful in several applications. We will illustrate this method in what follows.

The Lifshitz method, also called macroscopic approach, consists in considering the two interacting objects as continuous media with a dielectric response to electromagnetic fields. The dispersion forces are then considered the mutual interaction of dipoles oscillating at a given frequency. When the separation distance becomes bigger than a cut-off length depending on this frequency and the light speed, the attraction tends to decrease because the propagation time becomes of the same order as the oscillation period of the dipoles, the field emitted by one dipole interacting with another dipole with a different phase. This effect has first been pointed out by Casimir and Polder [15] and computed by Lifhitz using the quantum field theory [59]. Although this approach is of the greatest complexity, similar results can be obtained by using the Hamaker results, on the condition to replace the Hamaker constant by a pseudoconstant involving more parameters. This method is out of our scope, which is to roughly evaluate the importance of the van der Waals forces in microassembly and to investigate the influence of geometry, roughness, and orientation on the manipulation of microcomponents. We will therefore limit ourselves to the Hamaker method, despite its limitations. The interested reader will find further information about the Lifshitz approach in Adamson and Gast [1], Chapter VI, and in Israelachvili [39].

We present the Hamaker method to calculate the van der Waals forces in the case of the interaction between two spheres, a sphere and a infinite half-space, an infinite half-space limited by a smooth plane, and a rectangular box that has faces that are parallel or perpendicular to that plane. This last example is a good introduction for taking into account the influence of roughness. These results have been published in Lambert and Régnier [53].

In each case the Hamaker method consists in first determining the interaction potential W between two macroscopic objects [while $w(r)$ denotes the potential interaction between microscopic dipoles] and then in deriving it with respect to the separation distance D ($F = -dW/dD$).

1.2.1.1 Interaction Potential Between a Sphere and a Volume Element

The interaction potential $W_{(S,dV)}$ between a sphere S [center O, radius R, number density n_1 (m^3), volume element $d\Omega$] and a volume element dV (number density n_2) located at a distance D from the sphere is given by (see Fig. 1.2)

$$W_{(S,dV)} = -Kn_1n_2\,dV \int_{\Omega} \frac{1}{d^6} d\Omega \tag{1.10}$$

where d is the distance between dV and the volume element $d\Omega$ of S. Let us choose a spherical coordinate frame centered in O and a polar axis linking O and

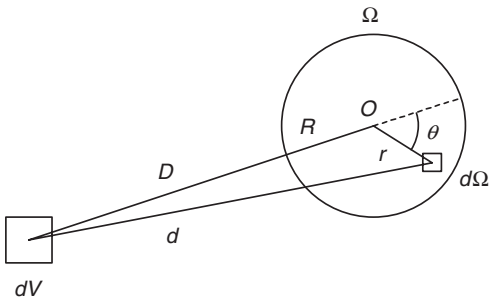

Figure 1.2. Interaction potential between a sphere and a volume element.

dV: Consequently, $d\Omega$ is located in the sphere by its distance r from O and the angle θ (the problem is symmetric as far as the azimutal angle ϕ is concerned). As a consequence, d is given by

$$d^2 = (D + R)^2 + r^2 + 2r(D + R)\cos\theta \tag{1.11}$$

and if we note $x = D + R$ the integral of Eq. 1.10 can be rewritten into

$$\int_{\Omega} \frac{1}{d^6} d\Omega = \int_0^{2\pi} d\phi \int_0^{\pi} d\theta \int_0^{R} \frac{r^2 \sin\theta}{(r^2 + x^2 + 2rx\cos\theta)^3}\, dr \tag{1.12}$$

$$= 2\pi \int_0^{R} dr \int_0^{\pi} \frac{r^2 \sin\theta}{(r^2 + x^2 + 2rx\cos\theta)^3}\, d\theta \tag{1.13}$$

The integral with respect to θ can be solved by assuming $\cos\theta = u$ (and thus $-\sin\theta\, d\theta = du$), leading to

$$\int_0^{\pi} \frac{r^2 \sin\theta}{(r^2 + x^2 + 2rx\cos\theta)^3}\, d\theta = \frac{r}{4x}\left[\frac{1}{(r - x)^4} - \frac{1}{(r + x)^4}\right] \tag{1.14}$$

and Eq. 1.13 is now given by

$$\int_{\Omega} \frac{1}{d^6} d\Omega = 2\pi \int_0^{R} \frac{r}{4x}\left[\frac{1}{(r - x)^4} - \frac{1}{(r + x)^4}\right] dr \tag{1.15}$$

$$= -\frac{4\pi}{3} \frac{R^3}{(R^2 - x^2)^3} \tag{1.16}$$

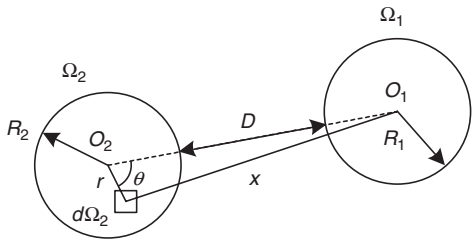

Figure 1.3. Interaction potential between two spheres.

Consequently, with the Hamaker constant $A \equiv Kn_1n_2\pi^2$[J], the interaction potential $W_{(S,dV)}$ of Eq. 1.10 is given by

$$W_{(S,dV)} = \frac{4AR^3}{3\pi[R^2 - (D+R)^2]^3}dV \tag{1.17}$$

1.2.1.2 Interaction Potential Between Two Spheres

In order to determine the interaction potential $W_{(S_1,S_2)}$ between two spheres S_1 (radius R_1, number density n_1, center O_1) and S_2 (radius R_2, number density n_2, center O_2) separated by a distance D (see Fig. 1.3), the interaction potential $W_{(S,dV)}$ of Eq. 1.17 must now be integrated over the second sphere:

$$W_{(S_1,S_2)} = \frac{4}{3\pi}AR_1^3 \int_{\Omega_2} \frac{1}{(R_1^2 - x^2)^3}\, d\Omega_2 \tag{1.18}$$

where $d\Omega_2$ is the volume element of S_2 and x is the distance between $d\Omega_2$ and O_1. Let us choose a spherical coordinates frame centered in O_2 with polar axis linking O_1 and O_2. The position of the volume element $d\Omega_2$ is defined by r, the distance between $d\Omega_2$ and O_2 and by θ, the angle between O_1O_2 and $O_2d\Omega_2$. The problem is again axially symmetric as far as the azimutal angle ϕ is concerned. As a consequence, by noting $R = R_1 + R_2 + D$, the distance x between O_1 and the volume element $d\Omega_2$ is given by

$$x^2 = R^2 + r^2 - 2rR\cos\theta \tag{1.19}$$

and Eq. 1.18 can be rewritten into[2]

$$W_{(S_1,S_2)} = \frac{4}{3\pi}AR_1^3 \int_0^{2\pi} d\phi \int_0^{R_2} dr \int_0^{\pi} \frac{r^2\sin\theta}{(R_1^2 - R^2 - r^2 + 2rR\cos\theta)^3} d\theta \tag{1.20}$$

$$= \frac{8}{3}AR_1^3 \int_0^{R_2} dr \int_0^{\pi} \frac{r^2\sin\theta}{(R_1^2 - R^2 - r^2 + 2rR\cos\theta)^3} d\theta \tag{1.21}$$

[2]$\log = \log_e = \ln \neq \log_{10}$.

$$= \frac{8}{3} A R_1^3 \int_0^{R_2} \frac{r}{4R} \left\{ \frac{1}{[R_1^2 - (R+r)^2]^2} - \frac{1}{[R_1^2 - (r-R)^2]^2} \right\} dr \quad (1.22)$$

$$= -\frac{A}{6} \left[\log \frac{R^2 - (R_1+R_2)^2}{R^2 - (R_1-R_2)^2} + \frac{2R_1R_2}{R^2 - (R_1+R_2)^2} + \frac{2R_1R_2}{R^2 - (R_1-R_2)^2} \right] \quad (1.23)$$

Equation 1.23 can also be written as follows:

$$W_{(S_1,S_2)} = -\frac{A}{6} \left[\log \frac{(R_1+R_2+D)^2 - (R_1+R_2)^2}{(R_1+R_2+D)^2 - (R_1-R_2)^2} + \frac{2R_1R_2}{(R_1+R_2+D)^2 - (R_1+R_2)^2} + \frac{2R_1R_2}{(R_1+R_2+D)^2 - (R_1-R_2)^2} \right] \quad (1.24)$$

$$= -\frac{A}{6} \left[\log \frac{D(2R_1+2R_2+D)}{(2R_1+D)(2R_2+D)} + \frac{2R_1R_2}{D(2R_1+2R_2+D)} + \frac{2R_1R_2}{(2R_1+D)(2R_2+D)} \right] \quad (1.25)$$

where D is the separation distance between the two spheres.

1.2.1.3 Potential Interaction Between a Sphere and an Infinite Half-Space

The interaction potential $W_{(S,HS)}$ between a sphere and an infinite half-space can be calculated as the limit of Eq. 1.24 when R_2 tends toward infinity:

$$W_{(S,HS)} = -\frac{A}{6} \left(\log \frac{D}{D+2R} + \frac{R}{D} + \frac{R}{2R+D} \right) \quad (1.26)$$

where D is the distance between the infinite half-space and the sphere and R is now the radius of the sphere.

1.2.1.4 Force Between Two Spheres

The force is calculated by deriving the interaction potential $W_{(S_1,S_2)}(D)$ given by Eq. 1.24 with respect to the separation distance D:

$$F_{(S_1,S_2)}(D) = \frac{A}{3}(R_1+R_2+D) \left[\frac{D(2R_1+2R_2+D) - 2R_1R_2}{D^2(2R_1+2R_2+D)^2} - \frac{D^2 + 2D(R_1+R_2) + 6R_1R_2)}{(2R_1+D)^2(2R_2+D)^2} \right] \quad (1.27)$$

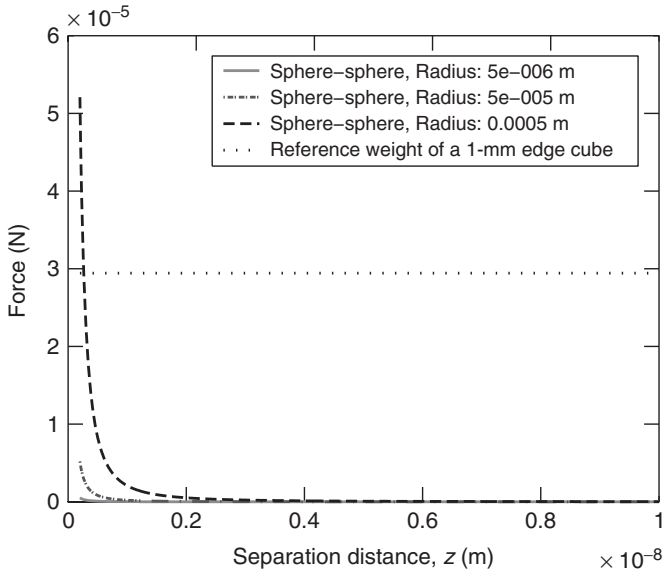

Figure 1.4. van der Waals force between two spheres with equal radii, Hamaker constant $= 5 \times 10^{-20}$ J. (As a comparison, the horizontal strip line represents the weight of a cube with a 1-mm edge and a density equal to 3000 kg m^{-3}, i.e., a bit heavier than aluminum.)

Moreover, if the separation distance D tends toward zero ($D << R_1$ and $z << R_2$), an approximation of $F_{(S_1,S_2)}(D)$ is given by

$$F_{(S_1,S_2)}(D) \approx -\frac{A\rho}{6D^2} \tag{1.28}$$

where $\rho = 1/R_1 + 1/R_2$.

An interesting result is that the force now depends on the inverse of the second power of the separation distance. The decrease consequently occurs more slowly, and the influence of van der Waals forces can be more seriously considered between two macroscopic objects (where macroscopic means "having a considerable number of molecules" but is still related to micrometric components). In order to have an idea of its order of magnitude, we plot the van der Waals forces as a function of the separation distance in Figure 1.4.

The numerical comparison between the analytical expression and its approximation is plotted in Figure 1.5: It can be concluded that the approximations can be widely used since the relative error is small: For objects with a characteristic size larger than a few microns and for separation distances smaller than 10nm (i.e., cut-off length to avoid the retardation effects that are not modeled in the described method), the relative error is smaller than 0.4% in all cases.

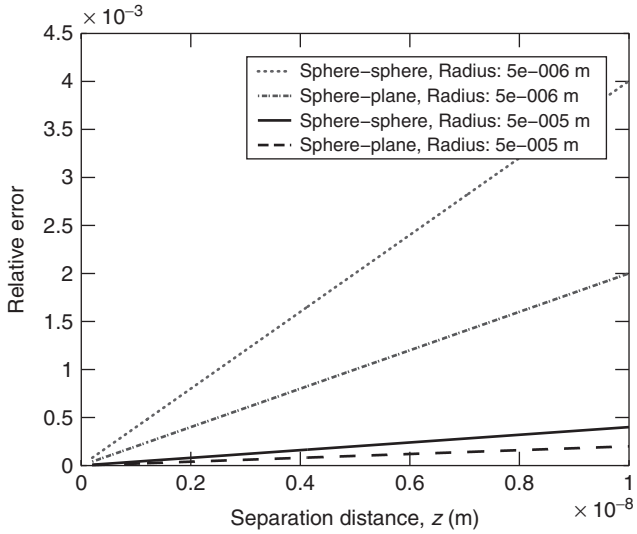

Figure 1.5. Relative errors between the analytical expressions and the approximations of the van der Waals forces.

1.2.1.5 Force Between a Sphere and an Infinite Half-Space

The force is calculated by deriving the interaction potential $W_{(S,HS)}(D)$ given by Eq. 1.26 with respect to the separation distance D:

$$F_{(S,HS)}(D) = -\frac{dW_{(S,HS)}(D)}{dD} = \frac{A}{6}\left[\frac{1}{D} - \frac{1}{2R+D} - \frac{R}{D^2} - \frac{R}{(2R+D)^2}\right] \tag{1.29}$$

Moreover, if D tends toward zero ($D << R$), an approximation of $F_{(S,HS)}$ is given by

$$F_{(S,HS)}(D) \approx -\frac{AR}{6D^2} \tag{1.30}$$

Note the similarity between Eqs. 1.28 and 1.30.

1.2.1.6 Interaction Between an Infinite Half-Space and a Rectangular Box

First, let us consider the interaction between a volume element dV_1 and an infinite half-space separated by a distance D such as the situation represented in Figure 1.6.

From Eq. 1.8, the interaction potential $w(z)$ between the volume element dV_1 containing n_1 molecules in cubic meters and a volume element dV_2 of the infinite

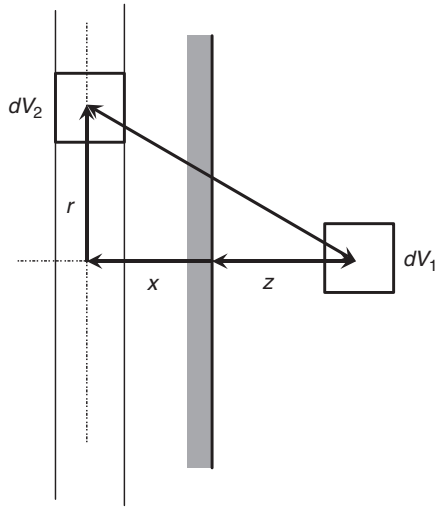

Figure 1.6. Interaction between a volume element and an infinite half-space.

half-space limited by a smooth plane and containing n_2 molecules in cubic meters is given by

$$w(z) = -\frac{n_1 n_2 K \, dV_1 \, dV_2}{d^6} \tag{1.31}$$

where d is the separation distance between dV_1 and dV_2. By choosing a coordinates frame centered in dV_1 whose z axis is perpendicular to the plane and by noting that $d^2 = z^2 + r^2$, this leads to the potential interaction between dV_1 and the half-space:

$$\begin{aligned} w(D) &= -2\pi K n_1 n_2 \, dV_1 \int_{z=D}^{z=\infty} dz \int_{r=0}^{r=\infty} \frac{r \, dr}{(z^2 + r^2)^3} \\ &= -\frac{A}{2\pi} \int_D^\infty \frac{dz}{z^4} = -\frac{A}{6\pi D^3} dV_1 \end{aligned} \tag{1.32}$$

where A is the well-known Hamaker constant already defined in a previous subsection. Henceforth, the force $f(z)$ between the half-space and the volume element is given by

$$f(z) = -\frac{\partial w}{\partial D} = -\frac{A}{2\pi D^4} dV_1 \tag{1.33}$$

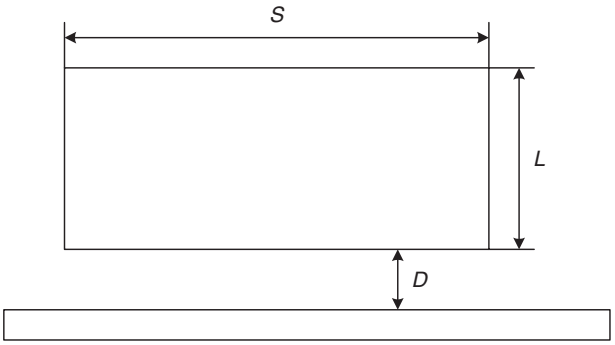

Figure 1.7. Interaction between rectangular box and infinite half-space.

We are now able to calculate the force between a given volume V_1 located near an infinite half-space limited by a smooth plane:

$$F = -\frac{A}{2\pi} \int_{V_1} \frac{1}{D^4} dV_1 \tag{1.34}$$

In the case of a rectangular smooth box with two faces of section S that are parallel to the plane (see Fig. 1.7), the force can be written as a function of materials (A), section (S), thickness (L), and separation distance (D):

$$F(A, S, L, D) = -\frac{AS}{2\pi} \int_{D}^{D+L} \frac{1}{z^4} dz = \frac{AS}{6\pi} \left[\frac{1}{(D+L)^3} - \frac{1}{D^3} \right] \tag{1.35}$$

Note that if $D << L$, Eq. 1.35 can be rewritten as a classical approximation [1]:

$$F(D) \approx -\frac{AS}{6\pi D^3} \tag{1.36}$$

Note that when the geometries become less obvious, the summation can no longer be achieved analytically. A method based on the Green identity is proposed in order to study the influence of the relative orientation of the objects and that of their roughness.

It proceeds as follows: The van der Waals force is computed by replacing the volume integral by a surface integral using the Green identity, as illustrated with the interaction between an infinite half-space and a rectangular box separated by a distance D [see Fig. 1.8(b)]. This problem has an analytical solution given by Eq. 1.35 that can be used to validate the method. This result will now be used in combination with the Green identity $\int_{\Omega} \int \int \operatorname{div} \overline{u}\, d\Omega = \oint_{\partial\Omega} \overline{u}.\overline{n}\, d(\partial\Omega)$. Let

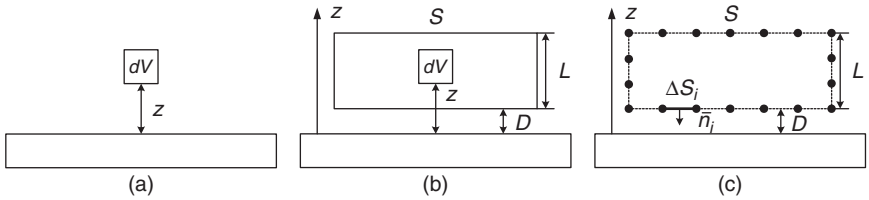

Figure 1.8. Geometry of the rectangular block: (a) infinite half-space and volume element, (b) geometry, and (c) mesh.

us assume a vector field given by $\overline{u} = -(1/3z^3)\overline{1}_z$. Its divergence is given by $\operatorname{div}\overline{u} = 1/z^4$. Consequently, Eq. 1.34 can now be rewritten as

$$F(D) = \frac{A}{2\pi} \oint_{\partial V_1} \frac{n_z}{3z^3}\, dS \tag{1.37}$$

Then, by meshing the surface of the considered object [see Fig. 1.8(c)] into N surface elements, the ith element being characterized by a normal vector with a z-component n_{zi}, the integral in Eq. 1.37 is replaced by a discrete sum:

$$F(D) = \frac{A}{6\pi} \sum_{i=1}^{N} \frac{n_{z_i}}{z^3} \Delta S_i \tag{1.38}$$

Examples of this method can be found in Lambert and Régnier [53] concerning the influence of the relative tilt of two parts and the influence of surface roughness modeled by a bearing curve.

As a summary of this section, let us indicate in Table 1.2 some useful approximations from the literature: additional references exist about the interaction between a sphere and a cylindric pore [73], between a sphere and a spherical cavity [85], and between two rough planes [33, 34].

As a conclusion there exist models: (1) without roughness no orientation [139], (2) with roughness but without orientation [2, 53, 90], and (3) without roughness but with orientation [23, 53]. Note that we have not found any description of a configuration that includes both roughness and orientation. Ideally, these forces should be computed again taking into account the mechanical deformations at contact. The proposed theory should be regarded as a first step.

To close this section, let us recall some useful references: [1, 12, 24, 38, 39, 53].

1.2.2 Capillary Forces

Capillary forces between two solids arise from the presence of a liquid meniscus between both solids. The presence of this liquid is due either to the

TABLE 1.2. Comparison Between the approximations from the Literature (D, separation distance, R the sphere radius, and A is the Hamaker constant)[a]

Object 1	Object 2	Expression	Reference
Plane	Plane //	$W \approx -\frac{A}{12\pi D^2}$; $F \approx \frac{A}{6\pi D^3}$ (by surface unit)	1,39,88
Cylinder	Cylinder //	$W \approx \frac{AL}{12\sqrt{2}D^3/2}\left(\frac{R_1R_2}{R_1+R_2}\right)^{1/2}$; $F \approx \frac{AL}{8\sqrt{2}D^{5/2}}\left(\frac{R_1R_2}{R_1+R_2}\right)^{1/2}$ (L, cylinders length; R_i, cylinders radii)	39, own results
Cylinder	Cylinder $\perp$	$W \approx -\frac{A\sqrt{R_1R_2}}{6D}$; $F \approx \frac{A\sqrt{R_1R_2}}{6D^2}$	1,39, own results
Sphere	Plane	$W \approx -\frac{AR}{6D}$; $F \approx \frac{AR}{6D^2}$	1,88
Sphere	Sphere	$W \approx -\frac{AR}{6D}$; $F \approx \frac{AR}{6D^2}$ (including conical and spherical asperities)	1,39,88

[a]Note that the minus sign of the forces has been omitted: they must be considered attractive.

user—who puts liquid to provoke an adhesion force, for example, to pick up a component—or due to the condensation of the surrounding humidity—either spontaneously due to environmental conditions or due to the cooling of a gripper, for example [18]. On a more general note, these forces arise from the surface tension of the interface between two media: water–air, water–oil, or oil–air. Therefore, they are also called surface tension forces or surface tension effects. They are of the utmost importance in the microworld because they clearly dominate all the other effects but maybe in some cases at a few nanometer scale the van der Waals forces with which they compete on a balanced manner.

Many aspects are worth mentioning: the underlying concepts, the models, the experimental measure, the applications, and the perspectives. Nevertheless, and it is not the scope of this book to detail all these aspects. The interested reader will find throughout this section many useful references on these topics. More generally, we refer to Lambert [50] for a detailed description of capillary forces in microrobotics (modeling, measurement, application to microassembly).

1.2.2.1 Key Concepts

The key concepts to the understanding and the modeling of capillary forces are the *surface energy*, *surface tension*, the *contact angles*, and *wettability* together with the *Young–Dupré equation*, the *pressure drop* across the interface described by the so-called *Laplace* equation, and the *curvature* of a surface in the three-dimensional (3D) space. Additional concepts are the *contact angle hysteresis*, the

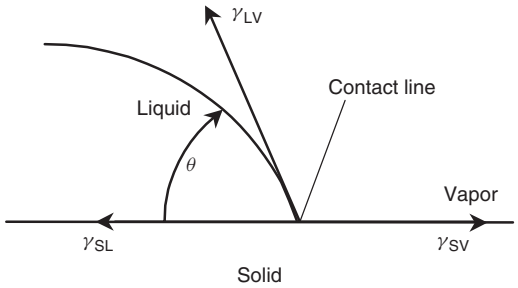

Figure 1.9. Illustration of the Young–Dupré equation.

surface impurities and *heterogeneities*, and the *dynamic spreading* of a liquid on a substrate.

Usually, if a liquid is not contained, it spreads out. However, when we look at soap bubbles or small water droplets, we observe that they behave as if their surface was an elastic membrane, characterized by a surface tension that acts against their deformations.[3] The concept of surface energy (or surface tension), which has the dimensions of an energy surface unit (J m^{-2}). The mechanical point of view considers the surface tension a tensile force by length unit (N m^{-1}). The surface tension is denoted by γ and its numerical value depends on the molecular interactions: in most oils, the molecular interaction is van der Waals interaction, leading to quite low surface tensions ($\gamma \approx 20$ mN m^{-1}). As far as water is concerned, due to the hydrogen bonding, the molecular attraction is larger ($\gamma \approx 72$ mN m^{-1}). Typical values for conventional liquid range from 20 mN m^{-1} (silicone oil) to 72 mN m^{-1} (water at 20°). For example, de gennes et al. [19] gives the following values for ethanol (23 mN m^{-1}), acetone (24 mN m^{-1}), and glycerol (63 mN m^{-1}).

Not only can the interface between a vapor and a liquid be characterized by an interfacial tension, denoted by γ and expressed as an energy surface unit or as a force by length unit, but the interfacial tensions can also be defined at the interfaces between a liquid and a solid (γ_{SL}) and between a solid and a vapor (γ_{SV}). Typical values of γ_{SV} are given in the literature [71]: nylon (polyamid) 6.6 (41.4 mN m^{-1}), high-density Polyethylene (PE) (30.3–35.1 mN m^{-1}), low-density PE (32.1–33.2 mN m^{-1}), Polyethylene terephthalate (PET) (40.9–42.4 mN m^{-1}), poly(methyl) methalcrylate (PMMA) (44.9–45.8 mN m^{-1}), Polypropylene (PP) (29.7), Polytetrafluoroethylene (PTFE) (20.0–21.8 mN m^{-1}).

The surface tension γ will indifferently be denoted by γ_{LV}. When a droplet is posed on a solid substrate (see Fig. 1.9), the liquid spreads out and we can distinguish three phases (vapor, liquid, solid) separated by three interfaces that join one another at the triple line, also called contact line.

At this triple line, the liquid–vapor interface makes an angle θ with the substrate. If the contact line is at equilibrium, θ is called the static contact angle,

[3]This is presented in a didactic way in de gennes et al. [19].

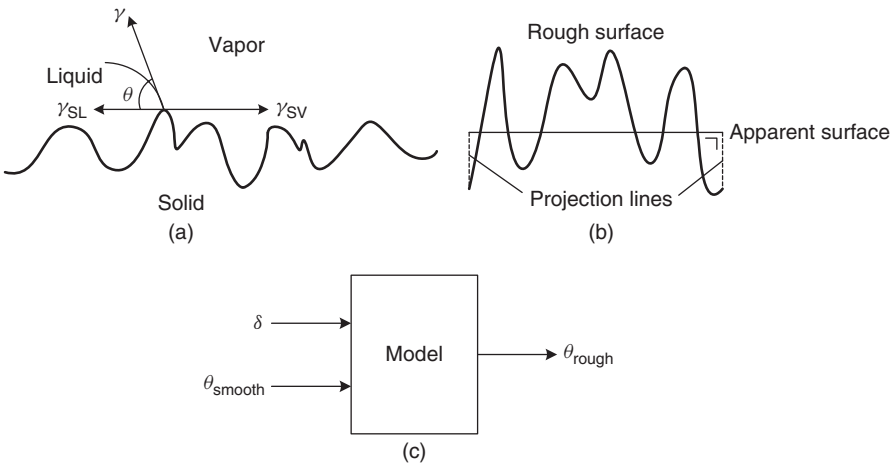

Figure 1.10. Influence of surface roughness: (a) contact line on a rough substrate, (b) actual and apparent surfaces, and (c) model to modify contact angle.

which is linked to the interfacial tensions by the Young–Dupré equation [1, 39]:

$$\gamma_{LV} \cos \theta + \gamma_{SL} = \gamma_{SV} \tag{1.39}$$

This equation can be written immediately by considering the balance of the forces acting on the contact line. A second approach is based on the fact that at equilibrium the energy must be extremal and that any displacement of the contact line leads to an energy variation equal to zero:

$$\begin{cases} \Delta G = \delta \, \Delta \, A(\gamma_{SL} - \gamma_{SV}) + \Delta A \gamma_{LV} \cos \theta \\ \lim_{\Delta A \to 0} \frac{\Delta G}{\Delta A} = 0 \end{cases} \tag{1.40}$$

where ΔA and ΔG are the variation of interface area and energy during the considered displacement. Let us now assume a heterogeneous surface containing two materials 1 and 2. A fraction f_1 of this surface is characterized by a surface energy leading to a contact angle θ_1, and the other part of the surface (fraction $f_2 = 1 - f_1$) leads to the contact angle θ_2. The theoretical contact angle given by the Young equation (1.39) is modified into an effective contact angle θ_C given by the Cassie equation [1, 40]:

$$\cos \theta_C = f_1 \cos \theta_1 + f_2 \cos \theta_2 \tag{1.41}$$

Another expression has been proposed by Israelachvili and Gee [40], but it seems that for the same values of θ_1, θ_2, f_1, and f_2, it will always predict a smaller contact angle than that obtained with Eq. (1.41):

$$(1 + \cos \theta_C)^2 = f_1(1 + \cos \theta_1)^2 + f_2(1 + \cos \theta_2)^2 \tag{1.42}$$

Let us assume a droplet placed on a rough substrate: Due to the roughness asperities, the actual area is bigger than the apparent one. Let us now introduce δ, the ratio of the actual interface area to the apparent one. The area of the actual (i.e., rough) area of the solid–vapor (solid–liquid) interface is denoted by A_{SV} (A_{SL}). The apparent surface is a projection of the rough surface:

$$\delta = \frac{A_{\mathrm{SL}}}{A_{\mathrm{Apparent}}} = \frac{A_{\mathrm{SV}}}{A_{\mathrm{Apparent}}} \tag{1.43}$$

Using δ, Eq. 1.40 can now be rewritten into

$$\begin{cases} \Delta G = \delta \Delta A_{\mathrm{Apparent}} \gamma_{\mathrm{SL}} - \delta \Delta A_{\mathrm{Apparent}} \gamma_{\mathrm{SV}} + \Delta A_{\mathrm{Apparent}} \gamma \cos\theta \\ \lim_{\Delta A \to 0} \dfrac{\Delta G}{\Delta A} = 0 \end{cases} \tag{1.44}$$

Combining Eqs. 1.44 and the expression of the contact angle given by the Young equation, the effective contact angle θ_{rough} can be expressed as a function of the surface ratio δ and the contact angle θ_{smooth} made of the liquid on a plane smooth substrate made of the same material:

$$\cos\theta_{\mathrm{rough}} = \delta \cos\theta_{\mathrm{smooth}} \tag{1.45}$$

This approach was first proposed by Wenzel [92] and more detailed information can be found in Adamson and Gast [1] and Hao et al. [29]. Henceforth, Eq. 1.45 can feed the previous simulation with contact angles corresponding to actual rough surfaces. That is important if the simulation is used to design gripper tips that usually present roughness profiles.

From Eq. 1.45, we see that angles lower than 90° are decreased by roughness, while the angle increases if θ is larger than 90°.

It must be noted that surface roughness can lead to condensing humid air in small cavities of the surface and hence to an attractive force L_{cp} due to liquid bridging [46]:

$$L_{\mathrm{cp}} = \frac{A_l \gamma}{r_k} \tag{1.46}$$

where A_l is the surface area where meniscus formation occurs and r_k is the Kelvin radius given by the Kelvin equation [1][4]:

$$r_k = \frac{\gamma v}{RT \log(p_0/p)} \tag{1.47}$$

where v is the molar volume of the liquid, R is the perfect gas constant, T is the absolute temperature, p_0/p is the relative vapor pressure (= relative humidity for water). Israelachvili [39] gives $\gamma v/RT = 0.54$ nm for water at 20°C.

[4] $\log = \log_e = \ln \neq \log_{10}$.

When the contact line is about to move, one observes the contact angle changing. The receding angle is smaller than the static angle while the observed angle, when moving forward, is larger than the static contact angle. A model has been proposed by Zisman (see Adamson and Gast [1]), who observed that $\cos\theta_A$ (advancing angle) is usually a monotonic function of γ. Henceforth, he proposed the following equation:

$$\cos\theta_A = a - b\gamma \tag{1.48}$$

Gutowsky [29] cited Johnson and Dettre [43] for a detailed study of the effect of roughness on contact angle hysteresis. This hysteresis implies that even at equilibrium, the contact angle value is not unique. The contact angle also depends on the velocity of the contact line. This phenomenon is described in Hoffman [36].

Due to the surface tension, there exists a pressure difference across the interface between a liquid and a gas. In the case of a soap bubble, for example, the pressure inside the bubble is bigger, to compensate the outside pressure and to overcome the tension effect. In a more general case, the pressure difference is linked to the curvature of the interface according to the Laplace equation [1]:

$$2\gamma H = 2\gamma\left(\frac{1}{R_1} + \frac{1}{R_2}\right) = p_{\text{in}} - p_{\text{out}} \tag{1.49}$$

where H is the mean curvature and R_1 and R_2 are two principal curvature radii.

1.2.2.2 Models of Capillary Forces

Models of capillary forces found in the literature are usually valid only at equilibrium. Before detailing them, let us now consider two solids linked by a liquid bridge,[5] also called meniscus (Fig. 1.11). In order to link this to the general frame of micromanipulation, let us call the upper solid the "tool" or the "gripper" (it will be used as a gripper) and the lower one as the object (it will be used as a micropart or a microcomponent). Since axial symmetry is assumed, it can be seen in Figure 1.11 that the contact line between the meniscus and the object (the gripper) is a circle with a radius r_1 (r_2). The pressure inside the meniscus is denoted by p_{in} and that outside the meniscus by p_{out}. The contact angle between the object and the meniscus is θ_1 and the angle between the gripper and the meniscus is θ_2. The separation distance (also called the gap) between the component and the gripper is denoted by z. The immersion height is called h. At its neck, the principal curvature radii are ρ' (in a plane perpendicular to the z axis, i.e., parallel to the component) and ρ (in the plane rz).

The object is submitted to the "Laplace" force, arising from the pressure difference $p_{\text{in}} - p_{\text{out}}$, and to the "tension" force, directly exerted by the surface

[5]The presented that is, configuration is axially symmetric, to introduce the capillary force from a "mechanical" point of view, that is, using concepts such as pressure or tension. In a more general case, the configuration is not axially symmetric and an energetic approach has to be implemented; see therefore Lambert [50].

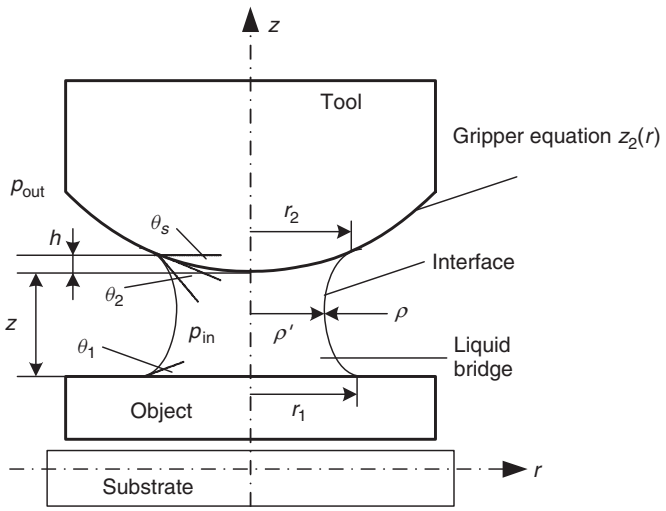

Figure 1.11. Effects of a liquid bridge linking two solid objects (from [52]).

tension. In what follows, we will consider that these two forces constitute what we will call the capillary force.[6] The Laplace force is due to the Laplace pressure difference that acts over an area πr_1^2 (see Fig. 1.12) and can be attractive or repulsive according to the sign of the pressure difference, that is, according to the sign of the mean curvature: A concave meniscus will lead to an attractive force while a convex one will induce a repulsive force.

$$F_{\mathrm{L}} = 2\gamma H \pi r_1^2 \tag{1.50}$$

The tension force implies the force directly exerted by the liquid on the solid surface. As illustrated in Figure 1.13, the surface tension γ acting along the contact circle must be projected on the vertical direction, leading to

$$F_{\mathrm{T}} = 2\pi r_1 \gamma \sin(\theta_1 + \phi_1) \tag{1.51}$$

Therefore, the capillary force is given by

$$F_C = F_T + F_L = 2\pi r_1 \gamma \sin(\theta_1 + \phi_1) + 2\gamma H \pi r_1^2 \tag{1.52}$$

where ϕ_1 denotes the slope of the component at the location of the contact line: It will be considered equal to zero in the following. In a more general way—for example, in the case of nonaxially symmetric geometries—the force is computed from the derivation of the surface energy. Both ways are proven to be equivalent [51]. Let us illustrate both methods in the following examples.

[6]Marmur [62] uses the terms "capillary" force for the term arising from the pressure difference and "interfacial tension force" for that exerted by the surface tension.

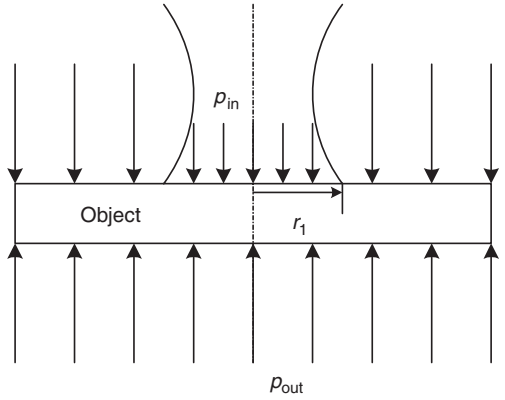

Figure 1.12. Origin of the Laplace force: attractive case (from [52]).

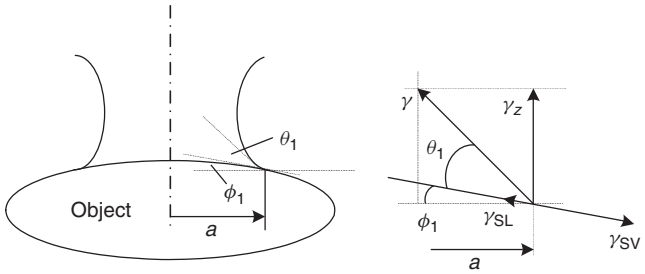

Figure 1.13. Origin of the tension force and detail (from [52]).

Surface Energy Derivation in the Case of a Sphere and a Plate. We detail here the mathematical developments required to calculate the analytical approximations of the capillary forces, based on energetic approach. Let us define preliminary mathematical formulations:

1. Definitions:

$$A(\phi) \equiv \frac{2\pi}{3}\left(1 - \frac{3}{2}\cos\phi + \frac{1}{2}\cos^3\phi\right)$$

$$\frac{dA}{d\phi} = \pi \sin^3\phi$$

2. Properties:

$$\cos\phi = 1 - \frac{\phi^2}{2} + \frac{\phi^4}{24} + O(\phi^6)$$

$$\cos^2\phi = 1 - \phi^2 + \frac{\phi^4}{3} + O(\phi^6)$$

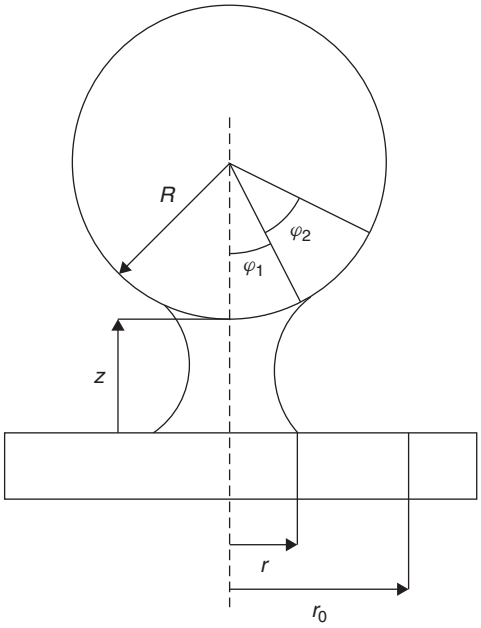

Figure 1.14. Studied configuration.

$$\cos^3\phi = 1 - \frac{3}{2}\phi^2 + \frac{7}{8}\phi^4 + O(\phi^6)$$

$$\sin\phi = \phi - \frac{\phi^3}{6} + O(\phi^5)$$

$$\sin^2\phi = \phi^2 - \frac{\phi^4}{3} + O(\phi^6)$$

$$\sin^3\phi = \phi^3 + O(\phi^5)$$

$$A(\phi) = \frac{\pi}{4}\phi^4 + O(\phi^6)$$

$$\frac{dA}{d\phi} = \pi\phi^3 + O(\phi^5)$$

$$1 - \cos\phi \approx \frac{\sin\phi^2}{2} \approx \frac{\phi^2}{2}$$

Now, let us compute the force between a sphere and a plane: The notations are defined in Figure 1.14. In this figure, ϕ_0 and r_0 are arbitrary constants. Their exact value does not play any role because the force will be calculated by deriving the interfacial energy W with respect to the gap z between the sphere and the

plane [39]:

$$F = -\frac{dW}{dz} \tag{1.53}$$

Let us write the interfacial energy of the system:

$$\begin{aligned} W(z) &= A_{\mathrm{SL}}\gamma_{\mathrm{SL}} + A_{\mathrm{SV}}\gamma_{\mathrm{SV}} + \Sigma\gamma \\ &= \gamma_{\mathrm{SL}}\pi r^2 + \gamma_{\mathrm{SV}}\pi(r_0^2 - r^2) + \gamma 2\pi r\big[z + R(1-\cos\phi)\big] \\ &\quad + \gamma_{\mathrm{SL}}2\pi R^2(1-\cos\phi) + \gamma_{\mathrm{SV}}2\pi R^2\big[(1-\cos\phi_0) - (1-\cos\phi)\big] \end{aligned} \tag{1.54}$$

Since ϕ is assumed to be small, W can be rewritten as

$$\begin{aligned} W(z) = \pi r^2(\gamma_{\mathrm{SL}} - \gamma_{\mathrm{SV}}) + \gamma 2\pi rz + \gamma\pi rR\,\sin^2\phi + \gamma_{\mathrm{SV}}\pi r_0^2 \\ + \pi R^2\,\sin^2\phi(\gamma_{\mathrm{SL}} - \gamma_{\mathrm{SV}}) + \gamma_{\mathrm{SV}}\pi R^2\,\sin^2\phi_0 \end{aligned}$$

and, by considering the Young–Dupré equation ($\gamma\,\cos\theta = -\gamma_{\mathrm{SL}} + \gamma_{\mathrm{SV}}$):

$$\begin{aligned} W = -2\pi R^2\,\sin^2\phi\gamma\,\cos\theta + \gamma_{\mathrm{SV}}\pi r_0^2 + \gamma 2\pi rz \\ + \gamma\pi R^2\,\sin^3\phi + \gamma_{\mathrm{SV}}\pi R^2\,\sin^2\phi_0 \end{aligned} \tag{1.55}$$

Let us now consider the derivative of W:

$$\begin{aligned} \frac{dW}{dz} = -4\pi R^2\,\sin\phi\,\cos\phi\gamma\,\cos\theta\frac{d\phi}{dz} + \gamma 2\pi R\,\sin\phi \\ + \gamma 2\pi zR\,\cos\phi\frac{d\phi}{dz} + 3\gamma\pi R^2\,\sin^2\phi\,\cos\phi\frac{d\phi}{dz} \end{aligned} \tag{1.56}$$

or, by assuming $\sin\phi \approx \phi$ and $\cos\phi \approx 1$:

$$\frac{dW}{dz} = -4\pi R^2\phi\gamma\,\cos\theta\frac{d\phi}{dz} + \gamma 2\pi R\phi + \gamma 2\pi Rz\frac{d\phi}{dz} + 3\gamma\pi R^2\phi^2\frac{d\phi}{dz} \tag{1.57}$$

The value of $d\phi/dz$ must be evaluated in Eq. 1.57. Therefore, the meniscus volume is assumed to be constant, leading to $dV/dz = 0$. Moreover the meniscus will be assumed to be cylindrically shaped so that the volume is the difference between the external liquid cylinder and the volume of the spherical cap inside the external cylinder:

$$V = \pi r^2\big[z + R(1-\cos\phi)\big] - \frac{2\pi R^3}{3}\Big(1 - \frac{3}{2}\cos\phi + \frac{\cos^3\phi}{2}\Big) \tag{1.58}$$

Once again the assumption of small ϕ is made, leading to the following approximation:

$$\frac{2\pi R^3}{3}\left(1-\frac{3}{2}\cos\,\phi+\frac{\cos^3\,\phi}{2}\right)=A(\phi)R^3\approx\frac{\pi R^3}{4}\phi^4 \tag{1.59}$$

The final expression for V is now given by

$$V=\pi r^2 z+\frac{\pi r^2 R}{2}\sin^2\,\phi-\frac{\pi R^3}{4}\phi^4 \tag{1.60}$$

$$=\pi R^2\,\sin^2\,\phi z+\frac{\pi R^3}{2}\sin^4\,\phi-\frac{\pi R^3}{4}\phi^4 \tag{1.61}$$

so that

$$\begin{aligned}\frac{dV}{dz}&=2\pi R^2 z\,\sin\,\phi\,\cos\,\phi\frac{d\phi}{dz}+\pi R^2\,\sin\,\phi\\&\quad+2\pi R^3\,\sin^3\,\phi\,\cos\,\phi\frac{d\phi}{dz}-\pi R^3\phi^3\frac{d\phi}{dz}\\&=2\pi R^2 z\phi\frac{d\phi}{dz}+\pi R^2\phi^2+\pi R^3\phi^3\frac{d\phi}{dz}\\&=0\\&\Rightarrow\frac{d\phi}{dz}=\frac{-\pi R^2\phi^2}{2\pi R^2\phi z+\pi R^3\phi^3}\\&=\frac{-1}{2z/\phi+R\phi}\end{aligned} \tag{1.62}$$

The total capillary force is then given by substituting this latter result into Eq. 1.57:

$$F=-\frac{4\pi R^2\phi\gamma\,\cos\,\theta}{2z/\phi+R\phi}-\gamma 2\pi R\phi+\frac{\gamma 2\pi Rz}{2z/\phi+R\phi}+\frac{3\gamma\pi R^2\phi^2}{2z/\phi+R\phi} \tag{1.63}$$

Since $h=R(1-\cos\,\phi)\approx(R/2)\sin^2\,\phi\approx(R/2)\phi^2$:

$$\begin{aligned}F&=-\frac{4\pi R\gamma\,\cos\,\theta}{2z/R\phi^2+1}-\gamma 2\pi R\phi+\frac{\gamma 2\pi Rz}{2z/\phi+R\phi}+\frac{3\gamma\pi R\phi}{2z/R\phi^2+1}\\&=-\frac{4\pi R\gamma\,\cos\,\theta}{z/h+1}-\gamma 2\pi R\phi+\frac{\gamma 2\pi Rz}{2z/\phi+R\phi}+\frac{3\gamma\pi R\phi}{z/h+1}\end{aligned}$$

The last three terms of this equation represent the contribution of the LV interface to the total interfacial energy. Let us assess their relative importance with respect to the first term. Their sum is given by

$$\frac{\pi R\gamma\phi(R\phi^2-2z)}{R\phi^2+2z} \tag{1.64}$$

The ratio of the first term to the sum of the last three ones is equal to

$$\frac{\frac{4\pi R\gamma\ \cos\theta}{z/h+1}}{\frac{\pi R\gamma\phi(R\phi^2-2z)}{R\phi^2+2z}} = \frac{4\ \cos\theta h}{\phi(h-z)} \tag{1.65}$$

If $z = 0$, this ratio tends toward infinity if ϕ tends to zero. Since ϕ cannot be exactly equal to zero, the last three terms can be neglected with the (now) classical assumption $\phi << .$ This leads to the well-known approximation [39]:

$$F_{\max} = -4\pi R\gamma\ \cos\theta \tag{1.66}$$

If $z \neq 0$ but by neglecting the contribution of lateral area to W, the total capillary force can be rewritten as follows:

$$F = -\frac{4\pi R\gamma\ \cos\theta}{z/h+1} \tag{1.67}$$

We see that this method requires one to assume a geometric shape for the meniscus. Numerical energy minimization techniques can be used to avoid this assumption, as implemented with finite elements in surface evolver. In this case, the method implementation is exact. Attention should, of course, be paid to the underlying assumptions of the model: constant volume of liquid (i.e., no evaporation), constant contact angles, static modeling, and vanishing Bond number (i.e., the gravity effect on the meniscus shape is neglected). *Note that these assumptions are restrictive for all models presented in this section*.

1.2.2.3 Direct Calculation of the Laplace and Tension Terms in the Case of Two Parallel Plates

Let us consider the configuration shown in Figure 1.15: Two parallel plates separated by a gap D are linked by a meniscus of volume V wetting the lower plate with a contact angle θ_1 and an upper plate with a contact angle θ_2. Since the configuration is axially symmetric, Eq. 1.49 can be rewritten using the expression of the curvature of an axially symmetric surface:

$$-\frac{r''}{(1+r'^2)^{3/2}} + \frac{1}{r(1+r'^2)^{1/2}} = \frac{\Delta p}{\gamma} \tag{1.68}$$

This a second-order nonlinear differential equation with a unknown second member. The initial condition are given by

$$r(z=0) = r_1 \tag{1.69}$$

$$r'(z=0) = -\frac{1}{\tan\theta_1} \tag{1.70}$$

The value of Δp can be adjusted to fit $r'(z=D) = 1/\tan\theta_2$ using a shooting method [50]. The initial radius r_1 can be iteratively guessed to adjust the volume

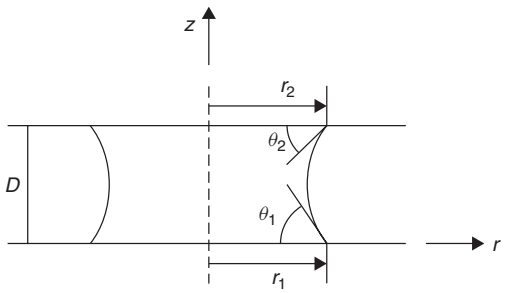

Figure 1.15. Axially symmetric meniscus between two parallel plates.

of liquid of the obtained meniscus equal to V. Thanks to this double iterative scheme, the meniscus shape and the pressure drop Δp can be known. Henceforth the force can be computed according to Equation 1.52.

It is interesting to note that in the case of a 2D configuration (different from the 2D axial symmetry), the curvature along the "extruding" direction perpendicular to the plane of this page is null. Equation 1.68 can be rewritten as

$$-\frac{r''}{(1+r'^2)^{3/2}} = \frac{\Delta p}{\gamma} \tag{1.71}$$

which corresponds to the equation of a circle (i.e., a 2D curve of constant curvature is the definition of a circle). The above-mentioned initial and boundary conditions can then be used to find the circle parameters (center coordinates and radius).

Finally, let us note that in the case of axially symmetric configurations, the meniscus can never be exactly a circle (since the term $1/[r(1+r'^2)^{1/2}]$ is different from zero). Nevertheless, the circle is a quite good approximation when the gap is small because in this case $r''/[(1+r'^2)^{3/2}] > 1/[r(1+r'^2)^{1/2}]$. This is the reason many authors assume the meniscus to be circular.

1.2.2.4 Other Models

Sphere–Sphere. Rabinovich [77] gives an analytical expression for the capillary force between two spheres with radii R_1 and R_2, as a function of the separation distance z:

$$F_{\text{sphere/sphere}} = -\frac{2R\cos\theta}{1+z/(2h)} \tag{1.72}$$

where R is the equivalent radius given by $R = 2R_1R_2/R_1 + R_2$, $2\cos\theta = \cos\theta_1 + \cos\theta_2$, z is the separation distance or gap, and h is the immersion height, approximately given by [77]

$$h = \frac{z}{2}[-1 + \sqrt{1 + 2V/(Rz^2)}] \tag{1.73}$$

where V is the volume of the liquid bridge.

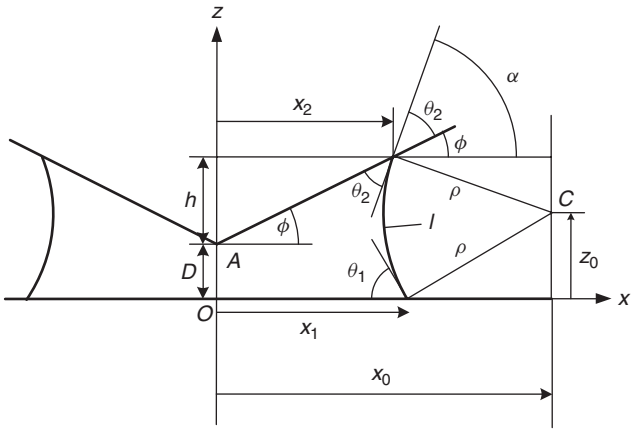

Figure 1.16. Prism–plane configuration.

Prism–Plane. In Lambert et al. [51] a model can be found for the interaction between a prism and a plate (Fig. 1.16). The prism is defined by its length in the y direction, L, and its angular aperture ϕ. Its location is defined by the distance[7] D between its apex A and the plane. Let us assume a volume of liquid V wetting the plane with a contact angle θ_1 and the prism with a contact angle θ_2. Since the curvature of the meniscus in the direction y perpendicular to $0xz$ is equal to zero, the Laplace equation becomes [52]

$$\frac{x''}{(1+x'^2)^{3/2}} = \frac{\Delta p}{\gamma} \tag{1.74}$$

where $x' = dx/dz$.

Assuming a vanishing Bond number, the hydrostatic pressure inside the meniscus is neglected by comparison to the Laplace pressure difference Δp, which is therefore constant in all the meniscus. Therefore, the second term of Eq. 1.74 is constant, and this equation can be integrated twice with respect to z in order to find the relation $x = x(z)$, with two integration constants and the undefined pressure difference Δp. A more straightforward derivation is based on the fact that since one of the curvature radius is infinite and that the total curvature $2H$ is constant, the second curvature radius $(1+x'^2)^{3/2}/x''$ is constant: Let us note it ρ. Therefore, the meniscus profile is a curve with constant curvature, that is, a circle given by the following equation:

$$(x - x_0)^2 + (z - z_0)^2 = \rho^2 \tag{1.75}$$

[7]For the sake of clarity, since z will be used as one of the coordinates, the gap is noted D in the following sections.

where x_0 and z_0 are the coordinates of the circle center. Once again, three parameters are to be determined: x_0, z_0, and ρ. This can be done using three boundary conditions: both contact angles θ_1 and θ_2 and the volume of liquid V.

As preliminary computations, let us express x_0, z_0, and ρ as functions of known data (ϕ,D,θ_1,θ_2) and the immersion height h, which is still unknown at this step, but which will be determined using the condition on the volume of liquid V. Note that x_2 is an intermediary variable and that x_1 will be used later. For the sake of convenience, the notation $\alpha = \theta_2 + \phi$ has been adopted in the following equations:

$$x_2 = \frac{h}{\tan \phi} \tag{1.76}$$

$$\rho = \frac{D + h}{\cos \theta_1 + \cos \alpha} \tag{1.77}$$

$$z_0 = \rho \cos \theta_1 \tag{1.78}$$

$$x_0 = x_2 - (z_0 - D - h) \tan \alpha \tag{1.79}$$

$$x_1 = x_0 - z_0 \tan \theta_1 \tag{1.80}$$

Additional useful relations are the meniscus equation:

$$x = x_0 - \sqrt{\rho^2 - (z - z_0)^2} \tag{1.81}$$

the meniscus slope x':

$$x' = -\frac{z - z_0}{x - x_0} \tag{1.82}$$

and, finally, the rewritten Laplace equation linking Δp and ρ:

$$\Delta p = \frac{\gamma}{\rho} \tag{1.83}$$

and h is still to be determined using the volume of liquid V (see next step).

The volume of liquid can be used to determine the value of the immersion height h, starting from the following expression of V as illustrated in Figure 1.17:

$$V = 2LA \tag{1.84}$$

$$= 2L[x_0(h + D) - A_{\mathrm{I}} - A_{\mathrm{II}} - A_{\mathrm{III}} - A_{\mathrm{IV}}] \tag{1.85}$$

where

$$A_{\mathrm{I}} = \frac{x_2 h}{2} \tag{1.86}$$

$$A_{\mathrm{II}} = \frac{(x_0 - x_2)(D + h - z_0)}{2} \tag{1.87}$$

$$A_{\mathrm{III}} = \frac{z_0(x_0 - x_1)}{2} \tag{1.88}$$

$$A_{\mathrm{IV}} = \frac{\rho^2(\pi - \alpha - \theta_1)}{2} \tag{1.89}$$

Therefore, the equation giving the volume V can be rewritten as follows:

$$\begin{aligned} V &= 2L\Bigg[x_0(D+h) - \frac{x_2 h}{2} \cdots \\ &\quad \cdots - \frac{\rho^2(\pi - \alpha - \theta_1)}{2} - \frac{(x_0 - x_2)(D + h - z_0)}{2} - \frac{z_0(x_0 - x_1)}{2}\Bigg] \end{aligned} \tag{1.90}$$

$$\begin{aligned} &= L\Bigg[2x_2 D + x_2 h \cdots \\ &\quad \cdots + \rho^2\Bigg[\sin\alpha\,\cos\alpha + 2\sin\alpha\,\cos\theta_1 - \pi + \alpha + \theta_1 - \sin\theta_1\cos(\theta_1) \end{aligned} \tag{1.91}$$

$$= L\left[h^2\left(\frac{1}{\tan\phi} + \mu\right) + 2hD\left(\frac{1}{\tan\phi} + \mu\right) + \mu D^2\right] \tag{1.92}$$

This latter equation can be rewritten as a second-degree equation with respect to the unknown h:

$$h^2 + 2hD + \frac{\mu D^2 - V/L}{\mu + 1/\tan\phi} = 0 \tag{1.93}$$

which leads to

$$h = -D \pm \sqrt{D^2 - \frac{D^2\mu - V/L}{\mu + 1/\tan\phi}} \tag{1.94}$$

The $-$ solution makes no physical sense since the immersion height cannot be negative. Consequently:

$$h = -D + \sqrt{D^2 - \frac{D^2\mu - V/L}{\mu + 1/\tan\phi}} \tag{1.95}$$

and the variation of h with respect to a variation of the separation distance D (it will be used in what follows) is given by

$$\frac{dh}{dD} = -1 + \frac{D}{D+h}\frac{1}{1 + \mu\,\tan\phi} \tag{1.96}$$

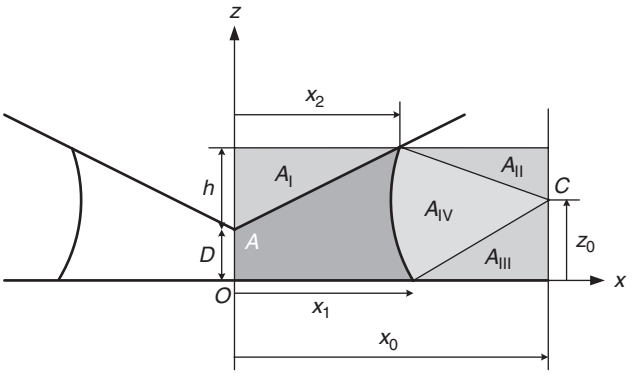

Figure 1.17. Determination of immersion height from volume of liquid.

As it has previously been explained, the capillary force can be written as the sum of a term depending on the Laplace pressure difference Δp and the so-called tension term:

$$F = 2Lx_1\,\Delta p + 2L\gamma\,\sin\,\theta_1 \tag{1.97}$$

$$= 2L\gamma\left(\frac{x_1}{\rho} + \sin\,\theta_1\right) \tag{1.98}$$

$$= 2L\gamma\frac{x_0}{\rho} \tag{1.99}$$

$$= 2L\gamma\left(\frac{x_2}{\rho} + \frac{D + h - z_0}{\rho}\tan\,\alpha\right) \tag{1.100}$$

$$= 2L\gamma\left(\frac{h}{D+h}\frac{\cos\,\theta_1 + \cos\,\alpha}{\tan\,\phi} + \sin\,\alpha\right) \tag{1.101}$$

Using Eq. 1.95, the force can be expressed as a function of the volume of liquid V, the separation distance D, and the angles of the problem: contact angles θ_1 and θ_2 at the one hand and the prism angle ϕ at the other hand. Remember that $\alpha = \theta_2 + \phi$. Lambert [50] explains how to adapt this model to the interaction between a cylinder and a plate. Additional information can be found in the literature [39, 48, 50].

1.2.2.5 Applications and Perspectives

Applications are based on the fact that surface tension is an important parameter in the perspective of a downscaling of the assembly equipment because the force it generates linearly decreases with the size while the weight decreases more quickly. While surface tension has been pointed out as being one of the disturbing effects in microelectromechanical systems (MEMS) (stiction problems [47, 63, 92], other uses have been positively considered [8, 32, 56, 70]. More particularly,

surface tension effects have been applied to many fields such as capillary gripping [4, 10, 28, 54, 69, 72, 84], fluidic microvalves [25], actuation [11], and optics [9].

The perspectives in this field are to model the force dynamically (level-set-based simulation packages can do some job), to exploit capillary condensation (see later on in this book).

1.2.3 Elastic Contact Mechanics

This subsection considers the Hertz contact theory and the related adhesion models [20, 35, 41, 67]. In case of a sphere (radius R) on a planar surface, pull-off force is approximately given by JKR (for the lower boundary) or DMT (for the higher boundary) contact models [20, 27]:

$$\frac{3}{2}\pi R W \leq F_{\text{pull-off}} \leq 2\pi R W \tag{1.102}$$

where W is the work of adhesion between the two media. According to Maugis [67], the λ coefficient can be used to choose the most appropriate contact model for a given case. This coefficient is expressed for an interface between two bodies 1 and 2 with

$$\lambda_{12} = 2\sigma_0 \left(\frac{R}{\pi W_{12} K^2} \right)^{1/3} \tag{1.103}$$

where K is the equivalent elastic modulus, calculated using the Poisson ratios μ and Young's modulus E:

$$K = \frac{4}{3}\left(\frac{1-\mu_1^2}{E_1} + \frac{1-\mu_2^2}{E_2} \right) \tag{1.104}$$

and W_{12} is expressed as $W_{12} = \gamma_1 + \gamma_2 - \gamma_{12} = 2\sqrt{\gamma_1 \gamma_2}$ with γ_{12} interfacial energy, γ_1 and γ_2 surface energy of the object, substrate, or tip [86]. Using λ, the pull-off force can be estimated with

$$\begin{aligned}
&\lambda < 0.1 \Longrightarrow \text{DMT model} \qquad P = 2\pi R W_{12} \\
&\lambda > 5 \Longrightarrow \text{JKR model} \qquad P = \frac{3}{2}\pi R W_{12} \\
&0.1 < \lambda < 5 \Longrightarrow \text{Dugdale model} \\
&\qquad P = \left(\frac{7}{4} - \frac{1}{4}\frac{4.04\lambda^{1/4} - 1}{4.04\lambda^{1/4} + 1} \right) \pi W_{12} R
\end{aligned} \tag{1.105}$$

When two media are in contact, the surface energy W_{12} is equal to

$$W_{12} \simeq 2\sqrt{\gamma_1 \gamma_2} \tag{1.106}$$

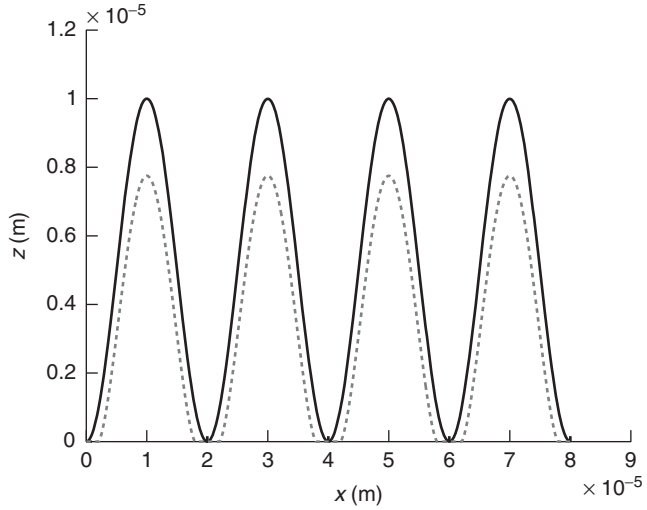

Figure 1.18. Wavy profile (solid line) and its deformation according to the Westegaard model.

with γ_i the surface energy of the body i. From the previous formulas the energy W_{132} required to separate two media 1 and 2 immersed in a medium 3 is given by

$$W_{132} = W_{12} + W_{33} - W_{13} - W_{23} = \gamma_{13} + \gamma_{23} - \gamma_{12}$$

Let us also cite the Westegaard model [42], which allows to compute the elastic deformation of a wavy surface against a infinite half-space. An example of the initial and deformed geometries is shown in Figure 1.18 Nevertheless, these models—which are widely used to interpret AFM measurements or to design grippers and microtools—rely on the elastic deformation assumption, which is usually no longer valid at scales smaller than 1 μm. Indeed, it can be shown from Table 1.3 that for example, in the case of a 0.600-μm diameter ball (the typical size for colloidal probes), the reference pressure p_0 always exceeds the elastic limit of 30 MPa (glass and silicon oxides). Consequently, we conclude the discrepancy of the Hertz model for balls with a diameter smaller that 1 μm. This implies that the other model does not hold either (DMT, JKR). This 1-μm limit cannot be put aside as far as CNT (carbon nanotubes) applications are concerned. Moreover, even for larger components, the roughness details are usually below this limit, which has a considerable impact on adhesion. Current research trends try to study the combined roles of plastic deformation and surface forces. More particularly, the interaction between roughness, plastic deformation, and electrostatic adhesion are fully described in Sausse Lhernould [81].

TABLE 1.3. Results of Some Hertz Model Computations ($E_1 = E_2 = 70$ Gpa, $\nu = 0.3$)

d (μm)	P (μN)	p_0
0.6	50	5 Gpa
0.6	5	2.5 Gpa
0.6	0.5	1.2 Gpa
0.6	0.05	0.5 Gpa
0.6	0.005	0.25 Gpa
60	0.005	11 Gpa
60	0.05	25 Gpa
60	0.5	54 Gpa

1.3 RECENT DEVELOPMENTS

1.3.1 Capillary Condensation

According to Mate [66], *one consequence of the pressure difference across a curved liquid surface is that the vapor pressure over a liquid surface depends on the degree of curvature of the surface. This leads to the phenomenon of capillary condensation, where vapors condense into small cracks and pores at vapor pressures significantly less than the saturation vapor pressure*. Capillary adhesion is an important source of perturbation in miniaturized systems. MEMS breakdown is often caused by adhesion problems [47, 63–65, 91]. Capillary condensation can be modeled thanks to the so-called Kelvin equation:

$$\frac{1}{r_1} + \frac{1}{r_2} = \frac{2}{r_k} = \frac{RT(P/P_s)}{\gamma V_m} \tag{1.107}$$

where r_1 and r_2 are the principal curvature radii, r_k is the so-called Kelvin radius, V_m the molar volume of the condensed liquid, γ the surface tension, R the perfect gas constant at 8.32 $\mathrm{J\,K^{-1}\,mole^{-1}}$, T the absolute temperature, P the vapor pressure over the curved liquid surface, and P_s the saturation vapor pressure over a flat surface. Note that the ratio P/P_s is equal to the relative humidity (RH), which ranges from 0 to 1 (corresponding to a range from 0 to 100%). Thanks to this model, the meniscus curvature can be known from the environmental parameters. It therefore becomes possible to compute a meniscus in the pore or crack or between a sharp AFM tip and the substrate. According to Mate [66], *for water,* $\gamma = 72\,\mathrm{mNm^{-1}}$ *and* $V_m = 18\,\mathrm{cm^3}$*, leading to* $r_k = -10$ nm *for* $P/P_s = 0.9$ *and* $r_k = -1$ nm *for* $P/P_s = 0.34$*. This means that for relative humidity between 34 and 90%, condensation of water vapor only forms a meniscus in nanometer-sized pores or gaps, that is, in those with diameters ranging from 2 to* 20 nm.

Inputing the meniscus curvature in Eq. 1.49, it becomes possible to compute the meniscus shape without knowing the volume of liquid (either the volume

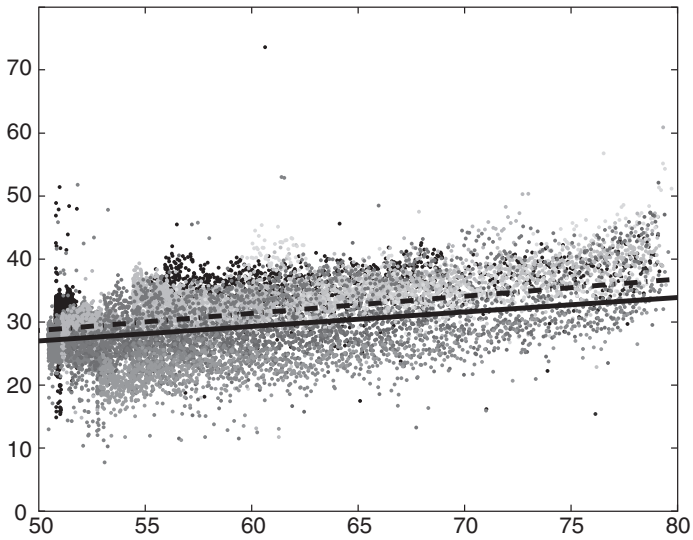

Figure 1.19. Pull-off force (nN) in function of the relative humidity (%): Comparison between model and experiment. The solid line has a slope determined with the model. The vertical position of the line (i.e, b from the $y = ax + b$ equation) has been chosen to best fit the points. The dashed line is the results of data fitting.

or the curvature must be known to solve the equation). As usual, the boundary condition of the differential problem (Eq. 1.49) is known from the contact angles. Using a finite-element resolution, Chau [16] has solved this problem for a full 3D geometry with 6 degrees of freedom of an AFM tip close to a flat surface. The pertinence of this problem has been pointed out by Sang et al. [80], confirming that capillary forces are of the first importance at the nanoscale (but also at all scales below the millimeter scale). The results of Chau [16] are twofold. First the model can predict quite well the experiment *on average*. This means that the large dispersion of the phenomenon can be mastered thanks to a large number of experiments. This allows one to confirm the validity of the Kelvin equation model at the scale of 10–100 nm. Second, the force increases with increasing humidity, and the dependence of the force on humidity is very sensitive to the tilt angle, that is, the relative orientation between the AFM tip and the substrate.

Note that the influence of roughness has not been modeled at this step; however, it is of the utmost importance as shown by very large dispersion of the experimental results.

Recent developments [5] show the influence of relative humidity. (Fig. 1.19) and the influence of the relative orientation between two solids (Fig. 1.20).

The importance of the tilt angle is also pointed out by Sang et al. [80], as indicated in Figure 1.21 (a colloidal probe is an AFM cantilever with a small sphere glued on it).

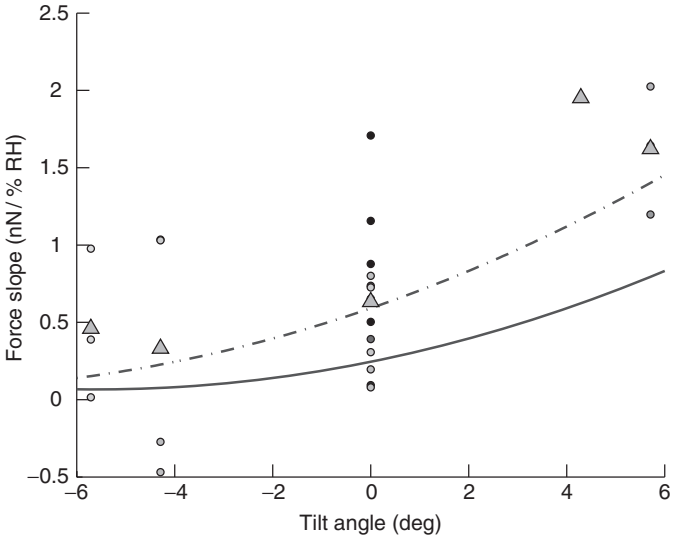

Figure 1.20. Comparison between model and experiment; the points are the slope of the force versus humidity slope; the solid line is the result of model computations for the same geometries. The tilt angle is given relatively to the tip support angle (12°). The dashed line is the result of the model for a tilt of 16°. Each point corresponds approximately to 300 measurements. The triangles are the means for each tilt angle value.

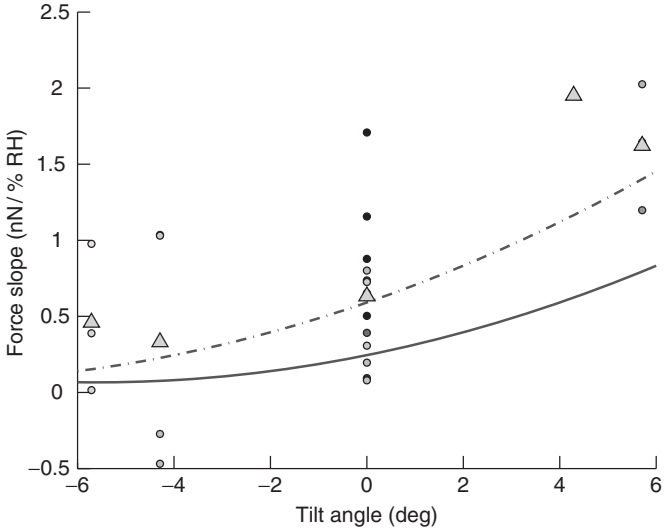

Figure 1.21. Measured pull-off force vs. wedge tilt angle. The result is highly sensitive to small changes of the tilt angle due to the effect of the colloidal probe roughness. A small change in the tilt angle causes a significant change in the pull-off force (from [80]).

TABLE 1.4. Terms Used in Chapter

Term	Definition	Units	Usual Values
ϵ_0	Free space permittivity	$C^{-2}\,N^{-1}\,m^{-2}$	8.85^{-12}
R	Sphere radius	m	10 nm to 100 μm
z	Separation distance	m	1 nm to 100 μm
V	Potential difference	V	0.5–20 V
θ	Cone half-aperture angle	rad	To 10°
L	Length of tip	m	10 μm to 500 μm
A	Area of contact	m^2	
r_{max}	Maximum distance to axis	m	
δ	Truncated cone height	m	
l	Plane width	m	
W	Electrostatic energy	J	
C	Capacitance	F	

1.3.2 Electrostatic Forces

This section could not have been written without the contribution of Marion Sausse-Lhernould [81].

Electrostatic forces between solids are also of importance at micro- and nanoscales. Basically, these forces come from the effect of electric fields on electrical charges. These charges can, for example, be acquired by tribo-electrification. The useful concepts—Coulomb's law, superposition principle, conductivity, permittivity, differences between electrostatics in free space and materials, differences between conductors and insulators, contact charging, polarization, induction, electrical breakdown, method of images also called mirror charges method—have been widely described in the literature [31, 44, 49, 57, 61, 68]. The goal of this section is therefore not to redevelop these theories. We prefer to present a summary of useful analytical models (see Table 1.5). Additionally, we will present some recent results based on Sausse Lhernould's work [81], studying the influence on electrical forces of surface roughness and mechanical deformation at contact.

Before reading through the summary table, let us recall the underlying assumptions. The main one for these analytical models is that surfaces are smooth for models not to take surface topography into account. This is a very strong assumption since, no matter how carefully or expensively a surface is manufactured, it can never be perfectly smooth. The second assumption defines materials as conductive where the potential is uniformly distributed along the surface, the electric field is normal to the surface, and the charges only carried by material surfaces (no volumic charges). The fact that no charge is present between the contacting objects is the third assumption. Table 1.4 summarizes and briefly defines the different terms used. In Figure 1.22 the different geometries involved in this work are presented: plane–plane contact, sphere–plane contact, sphere-ended cone–plane contact, and hyperbole–plane contact.

Let us now detail these analytical models.

TABLE 1.5. Review of Analytical Models

Contact Type	Expression	Reference
Plane–plane	$F_{\text{plane}} = \dfrac{\epsilon_0 V^2 A}{2z^2}$	22
Sphere–plane	$F_{\text{sphere1}} = \dfrac{\pi\epsilon_0 R V^2}{\vec{z}}$ for $R >> z$	6, 12, 14, 22
Sphere–plane	$F_{\text{sphere2}} = \dfrac{\pi\epsilon_0 R^2 V^2}{z^2}$ for $R << z$	14, 37
Sphere–plane	$F_{\text{sphere3}} = \pi\epsilon_0 \dfrac{R^2 U^2}{z(z+R)}$ for $R << z << L$	37, 13
Cylinder–plane	$F_{\text{cyl}}(\text{N/m}) = \dfrac{\pi\epsilon_0\epsilon_R\sqrt{R}V^2}{2\sqrt{2}z^{3/2}} = \dfrac{\pi\epsilon_0\epsilon_R\lambda V^2}{4\sqrt{2}\pi\sqrt{A}z^{3/2}}$	87
Conical tip	$F_{\text{ch}} \cong \dfrac{\lambda_0^2}{4\pi\epsilon_0}\ln\left(\dfrac{L}{4z}\right)$ for $R << z$	30
(charged line)	with $\lambda_0 = 4\pi\epsilon_0 V\left[\ln\left(\dfrac{1+\cos\theta}{1-\cos\theta}\right)\right]^{-1}$	
Conical tip	$F_{as} = \pi\epsilon_0 V^2\left\{\dfrac{R^2(1-\sin\theta)}{z\,[z+R(1-\sin\theta)]}\ \ldots\right.$	37
	$\left.+k^2\left[\ln\dfrac{L}{z+R(1-\sin\theta)} - 1 + \dfrac{R\cos^2\theta\,\sin\theta}{z+R(1-\sin\theta)}\right]\right\}$	
(asympt. model)	with $k^2 = 1/\{\ln[\tan(\theta/2)]\}^2$	
Hyperb. tip	$F_{\text{hyp1}} = \pi\epsilon_0 V^2 k^2\left[\ln\left(1+\dfrac{L}{R}\right) - \dfrac{(z - R/\tan\theta^2)L}{z(L+z)}\right]$	55
	with $k^2 = 1/\{\ln[\tan(\theta/2)]\}^2$	
Hyperb. tip	$F_{\text{hyp2}} = 4\pi\epsilon_0 V^2 \dfrac{\ln\left[1+(r_{\max}/R)^2\left(1+\dfrac{R}{z}\right)\right]}{\ln^2\left(\dfrac{1+\eta_{\text{tip}}}{1-\eta_{\text{tip}}}\right)}$	74, 75
	with $\eta_{\text{tip}} = \sqrt{\dfrac{z}{z+R}}$	

1.3.2.1 Plane–Plane and Sphere–Plane Models

Plane–plane and sphere–plane models are the most encountered in the literature. The expressions have been derived from the electrostatic energy $W(d)$.

$$F_{\text{elec}}(z) = -\frac{\partial W(z)}{\partial z} = -\frac{1}{2}\frac{\partial C}{\partial z}V^2 \tag{1.108}$$

The simple case [22] is the plane–plane contact where two smooth planar surfaces are brought into contact. The surface of contact has an area A and the capacitance

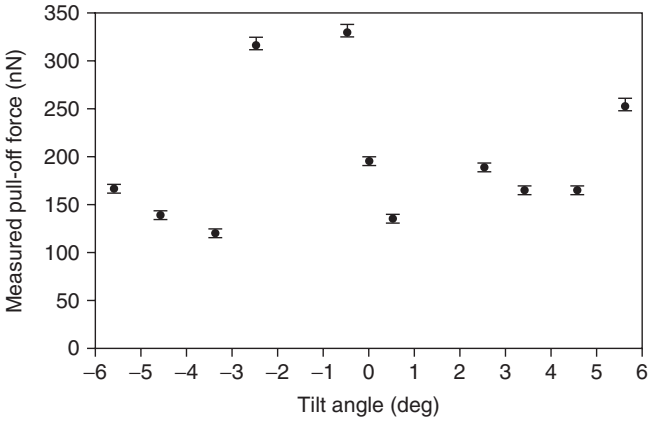

Figure 1.22. Representation of the involved geometries.

is obtained from the well-known plane capacitor case:

$$C(d) = \frac{\epsilon_0 A}{z}$$
$$F_{\text{plane}} = \frac{\epsilon_0 V^2 A}{2z^2} \tag{1.109}$$

This model gives the electrostatic pressure and knowing the area of the surface the electrostatic force can be deduced. Experience shows, however, that it is very difficult to determine the area of contact in real configurations. The planar model is thus very restricted in terms of applications. Moreover, studied objects are rarely totally flat. In application it may thus be used at very close separation distances between objects when the contact can be estimated by flat surfaces.

The sphere models have been developed for more complex shapes and longer separation distances. Many authors such as Krupp [49] have used them when studying the adhesion phenomenon disturbing micromanipulations. These models give an estimation of the electrostatic forces for the contact between a conductive sphere and a conductive plane. As the previous model, they are derived from the electrostatic interaction energy, and the capacitance between a sphere and a plane is given by the following expression:

$$C_{\text{sphere}} = 4\pi\epsilon_0 R \sinh(\alpha) \sum_{n=1}^{\infty} (\sinh n\alpha)^{-1}$$

with $\alpha = \cosh^{-1}[(R+z)/R]$. It is usual to analyze the contact between tip and surface in AFM as a sphere above a conducting plane [12]. The developed expressions depend on the separation distance and more precisely on the ratio between the sphere radius R and the separation distance z. Three models have

been developed from the general expression given by Durand [21], depending on the separation distance range.

For small separation distances the electrostatic force is proportional to the inverse of the separation distance [6, 12, 14, 22]:

$$F_{\text{sphere1}} = \frac{\pi \epsilon_0 R V^2}{z} \quad R >> z \tag{1.110}$$

For large separation distances, the electrostatic force is proportional to the inverse of the squared separation distance [14, 37]:

$$F_{\text{sphere2}} = \frac{\pi \epsilon_0 R^2 V^2}{z^2} \quad R << z \tag{1.111}$$

For all separation distances [13, 37] a general expression has been developed from Eqs. 1.110 and 1.111:

$$F_{\text{sphere3}} = \pi \epsilon_0 \frac{R^2 V^2}{z(z+R)} \tag{1.112}$$

These models are restricted in their applicable separation distances. They are often used to get a quantitave assesment of the electrostatic forces between the probe and the substrate in scanning probe microscopy.

1.3.2.2 Uniformly Charged Line Models (Conical Tip Models)

The principle consists in replacing the equipotential conducting surfaces by the equivalent image charges. The main hypothesis is that the cone may be approximated by a charged line of constant charge density λ_0 given by Hao et al. [30] for small aperture angle ($\theta \leq \pi/9$) by the expression

$$\lambda_0 = 4\pi \epsilon_0 V \left[\ln \left(\frac{1 + \cos \theta}{1 - \cos \theta} \right) \right]^{-1} \tag{1.113}$$

In the previous expression, θ is the half-aperture angle of the cone. The hypothesis implies that the charges are uniformly distributed on the conical object. This is only accurate if the objects are sufficiently placed appart from each other but is incorrect at small separation distances. The model is thus restricted to large separation distances:

$$F_{\text{uni}} \cong \frac{\lambda_0^2}{4\pi \epsilon_0} \ln \left(\frac{L}{4z} \right) \quad R << z << L \tag{1.114}$$

Our validations show that this model fits well the experimentally measured forces at large tip–sample separations.

1.3.2.3 The Asymptotic Model

The principle is to decompose a conical tip into infinitesimal surfaces [37]. The contribution of the apex and the spherical tip are evaluated separately and then added to get the total force. In this method the first step identifies the tip surface as a superposition of infinitesimal surfaces (facets). The first hypothesis is that from an electrostatic point of view, for distances larger than the characteristic facet dimensions, the surface is regular. The second step, which is also the second hypothesis, evaluates the electric field created between the facetted conductor and the plane surface by postulating that the electric field on each infinitesimal surface of the tip is equal to that created by the dihedral capacitance constituted by two infinite planes in the same relative orientation. The tip surface force is obtained by adding the contributions brought by each element. The expression is given by

$$F_{\text{asymp}} = \pi \epsilon_0 V^2 \left[\frac{R^2(1-\sin\theta)}{z\,[z + R(1-\sin\theta)]} + k^2 \left(\ln \frac{L}{z + R(1-\sin\theta)} - 1 + \frac{R\cos^2\theta/\sin\theta}{z + R(1-\sin\theta)} \right) \right] \tag{1.115}$$

with $k^2 = 1/\{\ln[\tan(\theta/2)]\}^2$. The validation has been performed by the authors being able to reestablish the well-known expressions for the sphere–plane contact.

1.3.2.4 The Hyperboloid Model (Hyperboloid Tip Model)

In this model the tip is represented by hyperboles bounded by a maximum distance $r_{\max}$ from the axis. The expression is derived by solving the Laplace equation in a prolate spheroidal coordinate system and by treating the tip–sample geometry as two confocal hyperboloids. Please refer to Patil and co-workers [74, 75] for calculation details. The boundary conditions are: the tip is at a potential V and the sample is grounded. The electric field and charge density are calculated using the boundary conditions. An integration on the surface allows to obtain the force. In this model the electrostatic force between tip and sample is given by

$$F_{\text{hyp}} = 4\pi\epsilon_0 V^2 \frac{\ln\left[1 + \left(\frac{r_{\max}}{R}\right)^2 \left(1 + \frac{R}{z}\right)\right]}{\ln^2\left(\frac{1+\eta_{\text{tip}}}{1-\eta_{\text{tip}}}\right)} \tag{1.116}$$

where $\eta_{\text{tip}} = \sqrt{z/z + R}$ and $r_{\max}$ is the cut-off radius introduced to avoid divergence. The validation is done through our own experimental measures. The theoretical and experimental results are in good agreement over distances ranging from 50 to 350 nm and voltages from 5 to 20 V. The limitation is mainly at very short interaction distances.

1.3.2.5 The Cylindrical Model

This model is different compared to the other because it is two-dimensionnal and not axisymetrical. Using the analytical model for the cylinder–plane contact [87], the electrostatic force is given by

$$F_{\text{elec}}^{\text{nondeformed}}(\text{N/m}) = \frac{\pi\epsilon_0\epsilon_R\sqrt{R}V^2}{2\sqrt{2}z^{3/2}} = \frac{\pi\epsilon_0\epsilon_R\lambda V^2}{4\sqrt{2}\pi\sqrt{A}z^{3/2}} \tag{1.117}$$

1.3.2.6 Tilted Conical Tip Models

The principle of this model is to find an analytical expression for the electrostatic force between a smooth plane and a tilted cantilever with a conical tip in electrostatic force microscopy [17]. The field lines between the objects are assumed to be approximated by segments of circles coming from the tip and ending on a point of the surface (Fig. 1.23). The electric potential decays linearly along these circular segments. If the distance between the two conducting objects is not larger than their physical dimension, the magnitude of the electric field is assumed to be given by $E = V/a$ (a being the arc length of the circular segment). The approximation is valid for small separation distances. The total force is the sum of the contributions brought by the truncated cone and by the spherical apex:

$$F(z) \cong \frac{\epsilon_0 V^2}{2}\int_S \frac{1}{a^2}dS \tag{1.118}$$

$$F_{\text{tilt}}^{\text{apex}}(z) = \frac{\pi\epsilon_0 V^2}{1 + f(2\theta)\times(z/R)^2}\left(\frac{R + z/2}{R - 2z}\right)^2 \times\left\{\frac{R - 2z}{z\left[1 + 2\tan^2(\theta)z/R\right]} + 2\ln\frac{4z}{2z + R + (R - 2z)\cos(2\theta)}\right\} \tag{1.119}$$

$$F_{\text{tilt}}^{\text{cone}}(d) = f_{\text{cone}}\epsilon_0 V^2\left[\ln\left(\frac{z - \delta/2 + L}{z + \delta/2}\right) - \sin\theta\frac{L - \delta}{z - \delta/2 + L}\frac{z - \delta/2}{z + \delta/2}\right] \tag{1.120}$$

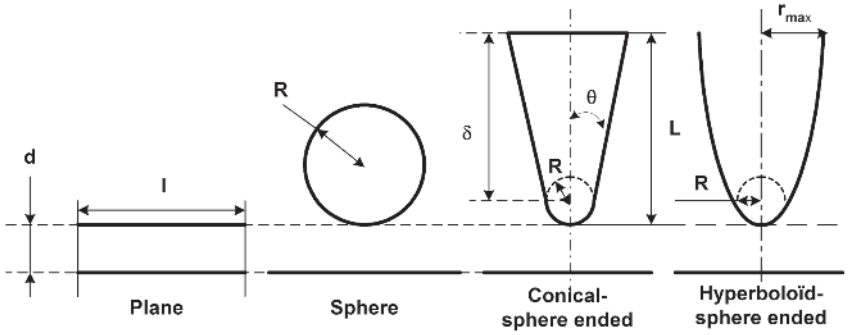

Figure 1.23. Tilted conical tip model, field lines are represented by segments of circle.

where $f_{\text{cone}} = 4\pi/(\pi - 2\theta)^2$, $f(2\theta) = \ln[1/\sin\theta]/([1 - \sin(\theta)][3 + \sin\theta])$, and $\delta = R/\tan^2\theta$.

Work taking into account the contribution of cantilever is found in the literature [17, 55].

1.3.2.7 Application to Scanning Probe Microscopy

The use of two models is recommended by Belaidi et al. [6] for the interaction between a tip and a planar surface in scanning probe microscopy: the spherical model for very short distances and the uniformly charged line model for longer distances. These two approximations correspond, respectively, to the case of an electrostatic force localized on the apex or on the conical side of the tip [55].

As indicated in the underlying assumptions of these analytical models, surface roughness is not taken into account. Sausse Lhernould and co-workers [81–83] have clearly shown the reduction of electrostatic forces in the presence of (even very small) surface roughness.

Indeed, a first comparison between simulation results [81] and literature results [79] is shown in Figure 1.24. The first observation is that even though results are in good correlation, simulated forces are stronger in smooth configuration than what was experimentally obtained. Moreover, the difference between experimental results and simulations increases when the separation distance decreases. This observation was attributed to the fact that even though the spot of contact has been chosen to be smooth, it can never be perfectly smooth. Even a very small roughness may influence the results at such small separation distances. Sausse Lhernould et al. [83] introduced roughness with the generation of a fractal surface using fractal parameters $D = 1.55$ and $G = 1.5 \times 10^{-12}$ for the planar contacting surface in order to have a maximum asperity peaks of 0.8 nm and an average roughness of 0.3 nm (which is often assumed to be negligible). The first observation is that even a roughness as small as this one is influencing the results from simulations, decreasing the electrostatic forces. This is specially true when the tip

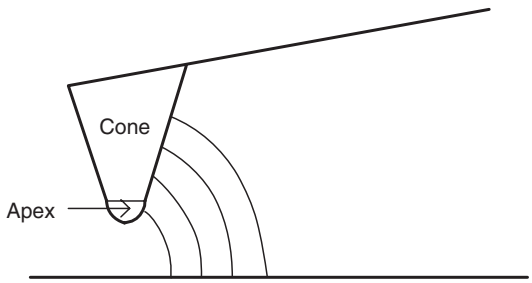

Figure 1.24. Comparison with experimental measures from Sacha et al. [79], who measured electrostatic forces for a sphere-ended conical tip of radius 40 nm and half-aperture angle 10° for different voltages. The characteristics of the tip were found using SEM images. The experimental results are compared with simulations, first without and then with roughness parameters (fractal representation).

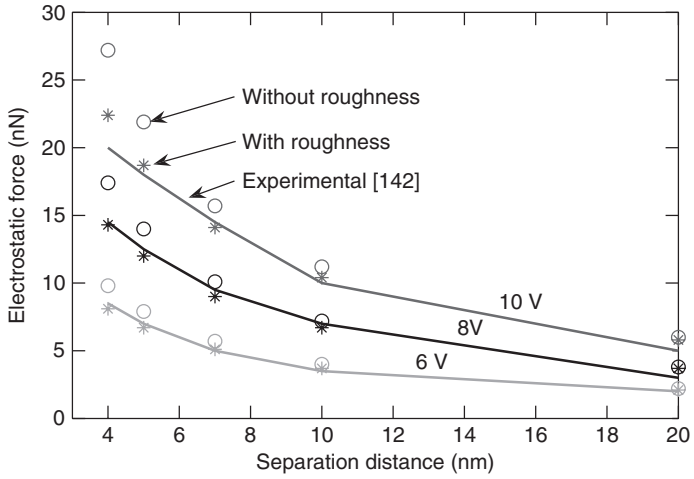

Figure 1.25. Electrostatic normal force (nN) vs. separation distance (nm) for a sphere-ended conical tip of radius 270 nm and half-aperture angle $\theta = 5^{\circ}$. Plot shows experimental results obtained by Hao et al. [30], simulation results without roughness parameters, and simulation results including different average roughness.

gets closer to the surface. The influence of surface roughness is also more important at higher applied voltages. The results from simulations including roughness are closer to the experimental measures.

Hao et al. [30] also measured electrostatic forces for a sphere-ended conical tip. The tip radius is 270 nm and the half aperture angle is 5°. Figure 1.25 shows experimental results obtained compared with simulations for different roughness parameters. Conclusions are identical to what was observed by Sacha et al. [79].

1.3.2.8 Impact of the Roughness

Sausse Lhernould [81] presents a comparison between numerical simulation and experimental force measurement (see Fig. 1.26). The force is computed and measured between a small conductive 10-μm sphere glued on an AFM cantilever (stiffness $= 0.942\ \mathrm{Nm}^{-1} \pm 17\%$) on the one hand and a conductive plane on the other hand. The sphere is assumed to be perfectly smooth while two different plane samples have been tested:

1. Sample A is: mechanical polishing of a nickel surface: $R_a = 2.49$ nm, $D = 1.218$, $G = 5.989 \times 10^{-20}$.
2. Sample B is: mechanical polishing of a nickel surface: $R_a = 13.55$nm, $D = 1.1355$, $G = 2.2261 \times 10^{-22}$.

We see in Figure 1.26 that both experimental curves indicate lower forces compared to the simulated smooth configuration. Second, we see that the correspondence between experiment and simulation is very good for the more rough sample

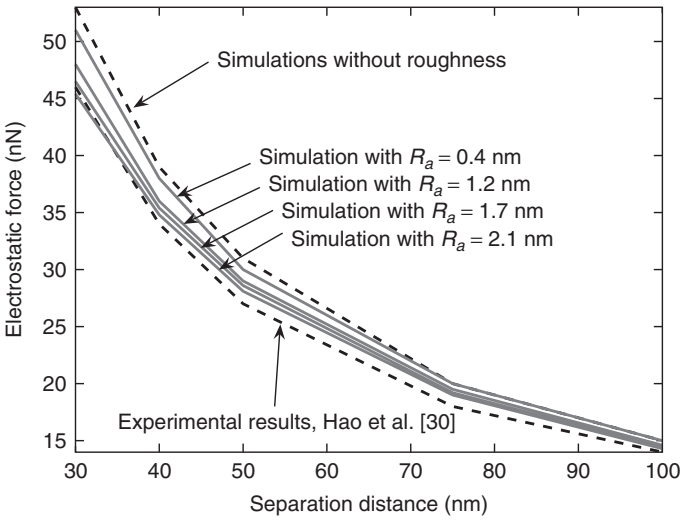

Figure 1.26. Comparison between experimental measures and numerical simulations for a 10-μm sphere approaching sample A and B for a 4-V voltage.

(B). The simulation is based on the Poisson equation solved in the free space around both solids, when a potential difference of 4 V is applied. The rough samples have been scanned and the fractal parameters D and G extracted from these profiles. Then, using the fractal function of Weierstrass–Mandelbrot with D and G, a rough plane geometry could be reconstructed before meshing and solving in COMSOL Multiphysics. In the case of sample A, which is smoother, the correspondence is not as good: the overestimation of the simulated force could come from the fact that the simulated geometry is 2D while the experimental measurement is done on a fully 3D configuration. Consequently, an isolated roughness peak on the actual sample will lead to a peak line in the simulation, overestimating the electrostatic force.

The justification why we claim the 2D simulation to overestimate the force is based on the following argument.

Let us first consider a 2D periodical rough profile, made of periods of length L. A fraction of L, fL, is the roughness peak. Consequently, the complementary $(1 - f)L$ is far away from the contact and its contribution to electrostatic force is neglected, due to the quick decrease of the force with increasing separation distances (cf. Eq. 1.106). Therefore, on a square of edge L, the force is equal to

$$F_{2D} = \frac{\epsilon_0 V^2}{2z^2} f L^2 \tag{1.121}$$

Let us now consider the same periodical surface in 3D: on a square of L^2 area, the peak area is now f^2L^2 while the $(1 - f)^2L^2$ does not contribute to the force (or has a vanishing contribution). Therefore, on this square of edge L, the force

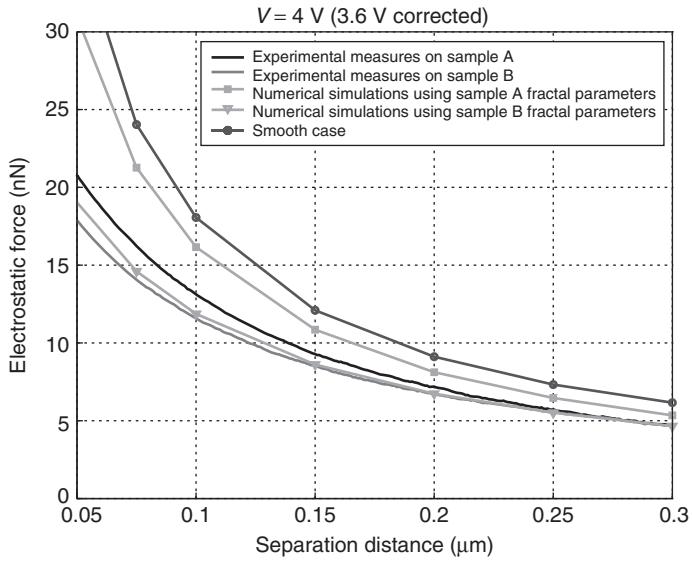

Figure 1.27. Qualitative influence of fractal roughness parameters D and G on the level force in the sphere–plane configuration (separation distance = 0.5 nm) for spherical object between 10 and 100 μm.

is equal to

$$F_{3D} = \frac{\epsilon_0 V^2}{2z^2} f^2 L^2 \tag{1.122}$$

Therefore, the ratio $F_{2D}/F_{3D} = 1/f$ is larger than 1, since f is smaller than 1. The prediction F_{2D} is larger than the actual force F_{3D}.

The influence of roughness on the electrostatic interaction can be estimated from the fractal dimension D and the fractal roughness parameter G (see Section 2.4 for details on roughness parametrization). This influence can be qualitatively estimated using the force reduction factor K given in Figure 1.27. This means that the force given by Eq. 1.110 (only at smaller separation distances) must be divided by K to take into account the effect of roughness. Since the K factor is given for a separation distance between the sphere and the plane equal to 0.5 nm, it cannot be applied to Eqs. 1.111 and 1.112.

Concerning the influence of mechanical deformation, a two-scale numerical study has been led in order to evaluate the effect of the surface roughness deformation on the adhesive electrostatic forces. The initial and deformed shapes of the considered profiles have been used in a numerical simulation to evaluate the adhesive electrostatic forces in a rough contact between two conductors. A large increase in the electrostatic forces between the initial undeformed and the final deformed configuration having a flat portion has been found. The adhesive forces are found to be up to 20 times larger in the deformed configuration (this may

lead to difficulties in releasing a manipulated object after micromanipulation). Closed-form expressions are proposed [81].

As a conclusion, we have shown in this section advanced results concerning electrostatic forces at the nano- and microscales. The conclusions to draw are manyfold:

1. The presence of surface roughness reduces the electrostatic force of a factor between 1 and 100. The effect of roughness can be estimated using numerical simulation and the roughness profile can be reconstructed from only two roughness parameters, namely the fractal parameters D and G. Note that the classical roughness parameter R_a has not been used in this study because it is not representative enough (as far as electrostatic effects are concerned).
2. The mechanical contact (which, e.g., occurs when picking a component) crushed the roughness asperities, leading to an electrostatic force increase up to $20\times$.
3. The correspondence between experiments and models is reasonably good when the potential difference between two *conductive* solids is *imposed*. In case of insulating material, the necessary model parameters such as the charges distribution cannot be known and henceforth no force can be computed.

REFERENCES

1. A. W. Adamson and A. P. Gast, *Physical Chemistry of Surfaces*, 6th ed., Wiley, New York, 1997.
2. F. Arai, D. Ando, T. Fukuda, Y. Nonoda, and T. Oota, Micro Manipulation Based on Micro Physics, in Proc. of IEEE/RSJ Conf. on Intelligent Robots and Systems, Vol. 2, Pittsburgh, 1995, pp. 236–241.
3. F. Arai and T. Fukuda, A New Pick up and Release Method by Heating for Micromanipulation, in IEEE Workshop on Micro Electro Mechanical Systems, Nagoya, Japan, 1997, pp. 383–388.
4. K.-B. Bark, *Adhésives Greifen von kleinen Teilen mittels niedrigviskoser Flissigkeiten*, Springer, New York, 1999.
5. N. Bastin, A. Chau, A. Delchambre, and P. Lambert, Effects of Relative Humidity on Capillary Force and Applicability of These Effects in Micromanipulation, in Poster at the Proc. of the IEEE/RSJ 2008 International Conference on Intelligent Robots and Systems, Nice, September 22–26, 2008.
6. S. Belaidi, P. Girard, and G. Leveque, Electrostatic Forces Acting on the Tip in Atomic Force Microscopy: Modelization and Comparison with Analytic Expressions, *J. Appl. Phys*., 81(3):1023–1029, 1997.
7. L. Benmayor, Dimensional Analysis and Similitude in Microsystem Design and Assembly, Ph.D. Thesis, Ecole Polytechnique Fédérale de Lausanne, 2000.
8. B. Berge, Electrocapillarité et mouillage de films isolants par l'eau, *Acad. Sci*., 317(II):157, 1993.

9. B. Berge and J. Peseux, Variable Focal Lens Controlled by an External Voltage: An Application of Electrowetting, *Eur. Phys. J. E*, 3:159–163, 2000.
10. F. Biganzoli, I. Fassi, and C. Pagano, Development of a Gripping System Based on Capillary Force, in Proceedings of ISATP05, Montreal, Canada, 19–21 July 2005, pp. 36–40.
11. R. T. Borno, J. T. Steinmeyer, and M. M. Maharbiz, Transpiration Actuation: The Design, Fabrication and Characterization of Biomimetic Microactuators Driven by the Surface Tension of Water, *J. Micromech. Microeng*., 16:2375–2383, 2006.
12. R. A. Bowling, A Theoretical Review of Particle Adhesion, in Proc. of Symposium on Particles on Surfaces 1: Detection, Adhesion and Removal, San Francisco, 1986, pp. 129–142.
13. H-J. Butt, B. Cappella, and M. Kappl, Force Measurements with Atomic Force Microscope: Technique, Interpretation and Applications, *Surf. Sci. Rep*., 59:1–152, 2005.
14. B. Cappella and G. Dietler, Force-Distance Curves by Atomic Force Microscopy, *Surf. Sci. Rep*., 34:1–104, 1999.
15. H. B. C. Casimir and D. Polder, The Influence of Retardation of the London–van der Waals Forces, *Phys. Rev*., 73(4):360, 1948.
16. A. Chau, Theoretical and Experimental Study of Capillary Condensation and of Its Possible Use in Micro-assembly—Etude théorique et expérimentale des forces dues Ãă la condensation capillaire, Ph.D. Thesis, Université libre de Bruxelles, 2007.
17. J. Colchero, A. Gile, and A. M. Baró, Resolution Enhancement and Improved Data Interpretation in Electrostatic Force Microscopy, *Phys. Rev. B*, 64:1–11, 2001.
18. M. Dafflon, Préhenseurs, conditions et stratégies pour une micromanipulation de précision, Ph.D. Thesis, EPFL, 2008.
19. P.-G. de Gennes, F. Brochart-Wyard, and D. Quéré, *Gouttes, bulles, perles et ondes*, Belin, 2002.
20. B. Derjaguin, V. M. Muller, and Y. P. Toporov, Effect of Contact Deformations on the Adhesion of Particles, *J. Colloid Interface Sci*., 53(2):314–326, 1975.
21. E. Durand, *Electrostatique: Tome II Problémes Généraux, Conducteurs*, Masson, 1966.
22. R. S. Fearing, Survey of Sticking Effects for Micro Parts Handling, in Proc. of IEEE/RSJ Conf. on Intelligent Robots and Systems, 5–9 August 1995, pp. 212–217.
23. J. T. Feddema, P. Xavier, and R. Brown, Micro-assembly Planning with van der Waals Force, in Proc. of IEEE Int. Symposium on Assembly and Task Planning, Porto, July 1999, pp. 32–38.
24. J. T. Feddema, P. Xavier, and R. Brown, Micro-assembly Planning with van der Waals Force, *J. Micromech*., 1(2):139–153, 2001.
25. Y. Feng, Z. Zhou, X. Ye, and J. Xiong, Passive Valves Based on Hydrophobic Microfluidics, *Sensors Actuators A*, 108:138–143, 2003.
26. R. J. Good, Theory of Adhesive Forces across Interfaces: 1. The Lifshitz–van der Waals Component of Interaction and Adhesion, in Lieng-Huan Lee, Ed., *Fundamentals of Adhesion*, Plenum, New York, 1991.
27. J. A. Greenwood and K. L. Johnson, An Adhesion Map for the Contact of Elastic Spheres, *J. Colloid Interface Sci*., 192(2):326–333, 1997.
28. H. Grutzeck, Fluidisches Greifen in der Mikrosystemtechnik, Ph.D. Thesis, TU Cottbus, 1999.

29. W. Gutowsky, Thermodynamics of Adhesion, in L. H. Lee, Ed., *Fundamentals of Adhesion*, Plenum, New York, 2001.
30. H. Hao, A. M. Baro, and J. J. Saenz, Electrostatic and Contact Forces in Force Microscopy, *J. Vacuum Sci. Technol. B*, 9(2):1323–1328, 1991.
31. W. Harper, *Contact and Frictional Electrification*, Clarenton Press, Oxford, UK, 1967.
32. B. H. W. Hendriks, S. Kuiper, M. A. J. Van As, C. A. Renders, and T. W. Tukker, Electrowetting-Based Variable-Focus Lens for Miniature Systems, *Opt. Rev*., 12(3):255–259, 2005.
33. M. C. Herman and K. D. Papadopoulos, *J. Colloid Interface Sci*., 136(2),385–392, 1990.
34. M. C. Herman and K. D. Papadopoulos, *J. Colloid Interface Sci*., 142(3),331, 1991.
35. H. Hertz, Uber die berihrung fester elastischer kirper, *J. Reine Angew. Math*., 92:156–171, 1882.
36. R. L. Hoffman, A Study of the Advancing Interface. I. Interface Shape in Liquid–Gas Systems. *J. Colloid Interface Sci*., 50(2):228–241, 1975.
37. S. Hudlet, M. Saint Jean, and J. Berger, Evaluation of the Capacitive Force between an Atomic Force Microscopy Tip and a Metallic Surface, *Eur. Phys. J. B*, 2:5–10, 1998.
38. J. N. Israelachvili, The Nature of van der Waals Forces, *Contemp. Phys*., 15(2):159–177, 1974.
39. J. N. Israelachvili, *Intermolecular and Surface Forces*, 2nd ed., Academic, London, 1992.
40. J. N. Israelachvili and M. L. Gee, Contact Angles on Chemically Heterogeneous Surfaces, *Langmuir*, 5(1):288, 1989.
41. K. L. Johnson, K. Kendall, and A. D. Roberts, Surface Energy and the Contact of Elastic Solids, *Proc. R. Soc. London Ser. A*, 324:301, 1971.
42. K. L. Johnson, *Contact Mechanics*, Cambridge University Press, London, 1985.
43. R. E. Johnson and R. H. Dettre, Contact Angle, Wettability and Adhesion, *Adv. Chem. Ser*., 43(8), 1998.
44. N. Jonassen, *Electrostatics*. Kluwer Academic, Amsterdam, 2002.
45. G. L. Klimchitskaya and V. M. Mostepanenko, Experiment and Theory in the Casimir Effect, *Contemp. Phys*., 47(3):131–144, 2006.
46. K. Komvopoulos, Surface Engineering and Microtribology for Microelectromechanical Systems, *Wear*, 200(1):305–327, 1996.
47. T. Kondo, S. Juodkazis, and H. Misawa, Reduction of Capillary Force for High-Aspect Ratio Nanofabrication, *Appl. Phys. A*, 81(8):1583–1586, 2005.
48. P. A. Kralchevsky and K. Nagayama, *Particles at Fluid Interfaces and Membranes*, Vol. 10 of *Studies in Interface Science*, Elsevier, New York, 2001.
49. H. Krupp, Particle Adhesion Theory and Experiment, *Adv. Colloid Interface Sci*., 1:111–239, 1967.
50. P. Lambert, *Capillary Forces in Microassembly: Modeling, Simulation, Experiments, and Case Study*, Microtechnology and MEMS, Springer, Boston, October 2007.
51. P. Lambert, A. Chau, A. Delchambre, and S. Régnier, Comparison between Two Capillary Forces Models, *Langmuir*, 24:3157–3163, 2008.

52. P. Lambert and A. Delchambre, Parameters Ruling Capillary Forces at the Submillimetric Scale, *Langmuir*, 21:9537–9543, 2005.
53. P. Lambert and S. Régnier, Surface and Contact Forces Models within the Framework of Microassembly, *J. Micromech*., 3(2):123–157, 2006.
54. P. Lambert, F. Seigneur, S. Koelemeijer, and J. Jacot, A Case Study of Surface Tension Gripping: The Watch Bearing, *J. Micromech. Microeng.,* 16(7):1267–1276, 2006.
55. B. M. Law and F. Rieutord, Electrostatic Forces in Atomic Force Microscopy, *Phys. Rev. B*, 66(035402-1), 2002.
56. J. Lee and C.-J. Kim, Surface-Tension-Driven Microactuation Based on Continuous Electrowetting, *J. Microelectromech. Syst.,* 9(2):171–180, 2000.
57. L.-H. Lee, The Chemistry and Physics of Solid Adhesion, in L.-H. Lee, Ed., *Fundamentals of Adhesion*, Plenum, New York, 1991.
58. C. Lenders, J. B. Valsamis, M. Desaedeleer, A. Delchambre, and P. Lambert, Assembly of a Micro Ball-Bearing Using a Capillary Gripper and a Microcomponent Feeder, in *Micro-Assembly Technologies and Applications*, International Precision Assembly Seminar (IPAS), Springer, Boston, 2008.
59. E. Lifshitz, *Sov. Phys.–JETP*, 73(2), 1956.
60. F. London, The London–van der Waals Attraction Between Spherical Particles, *Physica*, 4(10):1058–1072, 1937.
61. J. Lowell and A. Rose-Innes, Contact Electrification, *Adv. Phys.,* 29(6):947–1023, 1980.
62. A. Marmur, Tip-Surface Capillary Interactions, *Langmuir*, 9:1922–1926, 1993.
63. C. H. Mastrangelo, Mechanical Stability and Adhesion of Microstructures under Capillary Forces—Part I: Basic Theory, *J. Microelectromech. Syst.,* 2(1):33–43, 1993.
64. C. H. Mastrangelo, Surface Force Induced Failures in Microelectromechanical Systems, In Bharat Bhushan, Ed., *Tribology Issues and Opportunities in MEM*, pages 367–395. Kluwer Academic, Amsterdam, 1998, pp. 367–395.
65. C. H. Mastrangelo, Suppression of Stiction in MEMS, in *Spring MRS Meeting*, MRS, Boston, 1999.
66. C. M. Mate, *Tribology on the Small Scale*, Oxford University Press, Oxford, 2008.
67. D. Maugis, Adhesion of Spheres: The JKR-DMT Transition Using a Dugdale Model. *J. Colloid Interface Sci.,* 150(1):243–269, 1992.
68. A. D. Moore, *Electrostatics and Its Applications*, Wiley, New York, 1973.
69. K. J. Obata, T. Motokado, S. Saito, and K. Takahashi, A Scheme for Micromanipulation Based on Capillary Force, *J. Fluid Mech.,* 498:113–121, 2004.
70. K. W. Oh and C. Ahn, A Review of Microvalves, *J. Micromech. Microeng.,* 16(5):R13–R39, 2006.
71. U. Ohlerich, Tension superficielle, interfaciale et angle de contact, in Workshop, Anvers, 15 October 2002.
72. C. Pagano, L. Zanoni, I. Fassi, and F. Jovane, Micro-assembly: Design and Analysis of a Gripper Based on Capillary Force, in *Proc. of the 1st CIRP—International Seminar on Assembly Systems*, Stuttgart, Germany, 15–17 November 2006, pp. 165–170.
73. K. D. Papadopoulos and C.-C. Kuo, *Colloids Surf.,* 46(115), 1990.

74. S. Patil and C. V. Dharmadhikari, Investigation of the Electrostatic Forces in Scanning Probe Microscopy at Low Bias Voltage, *Surf. Interf. Anal.,* 33:155–158, 2002.
75. S. Patil, A. V. Kulkarni, and C. V. Dharmadhikari, Study of the Electrostatic Force between a Conducting Tip in Proximity with a Metallic Surface: Theory and Experiment, *J. Appl. Phys.,* 88(11):6940–6942, 2000.
76. J. Peirs, Design of Micromechatronic Systems: Scale Laws, Technologies, and Medical Applications, Ph.D. Thesis, KUL, Belgium, 2001.
77. I. Rabinovich, S. Esayanur, and M. Mougdil, Capillary Forces between Two Spheres with a Fixed Volume Liquid Bridge: Theory and Experiment, *Langmuir*, 21:10992–109927, 2005.
78. W. B. Russel, D. A. Saville, and W. R. Schowalter, *Colloidal Dispersions*, Cambridge University Press, Cambridge, UK, 1989.
79. G. M. Sacha, A. Verdaguer, J. Martinez, J. J. Séenz, D. F. Ogletree, and M. Salmeron, Effective Radius in Electrostatic Force Microscopy, *Appl. Phys. Lett.,* 86:123101, 2005.
80. S. Sang, H. Zhang, M. Nosonovsky, and K. Chung, Effects of Contact Geometry on Pull-off Force Measurements with Colloidal Probe, *Langmuir*, 24:743–748, 200.
81. M. Sausse Lhernould, Theoretical and Experimental Study of Electrostatic Forces Applied to Micromanipulation: Influence of Surface Topography, Ph.D. Thesis, Université libre de Bruxelles, 2008.
82. M. Sausse Lhernould, A. Delchambre, S. Régnier, and P. Lambert, Electrostatic Forces and Micromanipulator Design: On the Importance of Surface Topography Parameters, in Proceeding of the 2007 IEEE/ASME International Conference on Advanced Intelligent Mechatronics, 2007.
83. M. Sausse Lhernould, A. Delchambre, S. Régnier, and P. Lambert, Electrostatic Forces in Micromanipulations: Review of Analytical Models and Simulations Including Roughness, *Appl. Surf. Sci.,* 253:6203–6210, 2007.
84. D. Schmid, S. Koelemeijer, J. Jacot, and P. Lambert, Microchip Assembly with Capillary Gripper, in Proc. of the 5th International Workshop on Microfactories (4 pages), October 2006, pp. 25–27.
85. A. K. Segupta and K. D. Papadopoulos, Vander Waals Interaction between a Colloid and its Host Pore, *J. Colloid Interface Sci.,* 152(2):534–542, 1992.
86. M. Sitti and H. Hashimoto, Teleoperated Touch Feedback from the Surfaces at the Nanoscale: Modelling and Experiments, *IEEE-ASME Trans. Mechatron.,* 8(1):1–12, 2003.
87. W. R. Smythe, *Static and Dynamic Electricity*, McGraw-Hill, New York, 1968.
88. M. van den Tempel, *Adv. Colloid Interface Sci.,* 3(137), 1972.
89. R. Van Hauwermeiren, Cours d'électricité générale, Cours de 2éme candidature, ULB, 1993.
90. B. Vogeli and H. von Kanel, AFM Study of Sticking Effects for Microparts Handling, *Wear*, 238(1):20–24, 2000.
91. K. D. Vora, A. G. Peele, B.-Y. Shew, E. C. Harvey, and J. P. Hayes, Fabrication of Support Structures to Prevent su-8 Stiction in High Aspect Ratio Structures, *Microsyst. Technol.,* 2006.

92. R. N. Wenzel, Resistance of Solid Surfaces to Wetting by Water, *Industrial and Engineering Chemistry*, 28(8):988–994, 1986.
93. D. Wu, N. Fang, C. Sun, and X. Zhang, Stiction Problems in Releasing of 3d Microstructures and Its Solution, *Sensors Actuators A*, 128:109–115, 2006.
94. B. Yang and Q. Lin, A Latchable Microvalve Using Phase Change of Paraffin Wax, *Sensors Actuators A*, 134:194–200, 2007.